FUNCTIONALIZATION AND THICKNESS DEPENDENT PROPERTIES OF SINGLE LAYER DICHALCOGENIDES

A Thesis Submitted to
the Graduate School of Engineering and Sciences of
İzmir Institute of Technology
in Partial Fulfillment of the Requirements for the Degree of
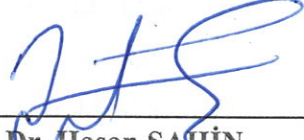
MASTER OF SCIENCE

in Photonics Science and Engineering
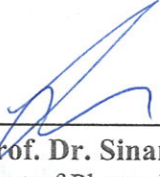
by
Zeynep KAHRAMAN

December 2019
İZMİR
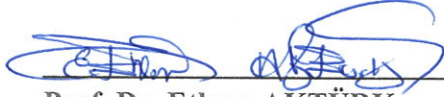
We approve the thesis of **Zeynep KAHRAMAN**
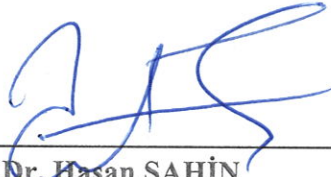
Examining Committee Members:

_____
Prof. Dr. Hasan ŞAHİN
Department of Photonics, İzmir Institute of Technology

_____
Assoc. Prof. Dr. Sinan Balcı
Department of Photonics, İzmir Institute of Technology
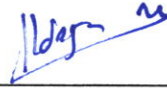
_____
Prof. Dr. Ethem AKTÜRK
Department of Physics, Aydın Adnan Menderes University

18 December 2019

_____
Prof. Dr. Hasan ŞAHİN
Supervisor, Department of Photonics,
İzmir Institute of Technology

_____
Assoc. Prof. Dr. Yaşar AKDOĞAN
Co-Supervisor, Department of
Material Science and Engineering,
İzmir Institute of Technology

_____
Prof. Dr. Canan VARLIKLI
Head of the Department of Photonics

_____
Prof. Dr. Mehtap EANES
Dean of Graduate School of
Engineering and Science

ACKNOWLEDGMENTS

ABSTRACT

FUNCTIONALIZATION AND THICKNESS DEPENDENT PROPERTIES OF SINGLE LAYER DICHALCOGENIDES

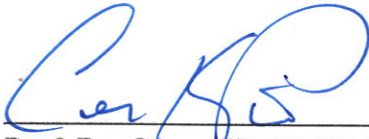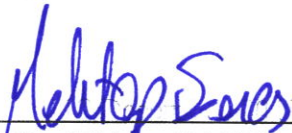After successful isolation of graphene in 2004, it was found that the layered materials showed different properties when diluted to the monolayer. The layer dependent structural, electronic and vibrational properties of the 1T phase of two dimensional (2D) platinum diselenide are investigated by means of state-of-the-art first-principles calculations.

In addition ultra-thin two-dimensional Janus type platinum dichalcogenide crystals formed by two different atoms at opposite surfaces are investigated by performing state-of-the-art density functional theory calculations. While all Janus structures are indirect band gap semiconductors as their binary analogs, their Raman spectra show distinctive features that stem from broken out-of-plane symmetry. Moreover, it was shown that vertically stacked van der Waals heterostructures of binary and ternary (Janus) platinum dichalcogenides offer wide-range electronic features by forming bilayer heterojunctions of type-I, type-II and type-III.

On the other hands, *Ab initio* calculations are performed in order to investigate the structural, vibrational, electronic, and piezoelectric properties of both bare TaS_2 and its functionalized structures. Furthermore, the elastic and piezoelectric properties of TaS_2 and its derivatives are analyzed. It is revealed that the in-plane piezoelectricity of TaS_2 can be enhanced via one-surface fluorination while an additional degree of freedom for the piezoelectricity can be added in all Janus structures due to the broken out-of-plane symmetry.

This thesis provides some important results understanding of thickness and functionalization dependent mechanics, vibrational, electronic properties of 2D materials.

ÖZET

TEK KATMANLI DİKALKOGENİDLERİN İŞLEVSELLEŞTİRME VE KALINLIĞA BAĞLI ÖZELLİKLERİ

2004'te grafenin başarılı bir şekilde izole edilmesinin ardından katmanlı malzemelerin mono tabakaya inceltildiğinde farklı özellikler gösterdiği ortaya çıkmıştır. 1T fazına sahip iki boyutlu (2D) $PtSe_2$'nin katmana bağlı olarak yapısal, elektronik ve titreşimsel özellikleri, temel prensiplere dayanan yoğunluk fonksiyonel teorisi (DFT) bazlı hesaplamalar vasıtasıyla incelenmiştir.

Ek olarak karşılıklı yüzeylerinde iki farklı atom tarafından oluşturulan, Janus tipi, ultra-ince iki boyutlu platin dikalgojenit kristalleri de temel prensiplere dayanan yoğunluk fonksiyonel teorisi hesaplamaları yapılarak incelenmiştir. Tüm Janus yapıları, ikili analogları gibi dolaylı bant aralığına sahip yarı iletkenler olsa da, Raman spektrumları, düzlem dışı simetriden kaynaklanan belirgin özellikler gösterir. Ayrıca, dikey olarak istiflenmiş ikili ve üçlü (Janus) platin dikalgojenitlerin van der Waals heteroyapıları tip I, tip II ve tip III heteroeklemleri oluşturarak, çok çeşitli elektronik özellikler sundukları gösterilmiştir.

Bunların yanısıra, hem TaS_2'nin hem de fonksiyonel yapılarının yapısal, titreşimsel, elektronik ve piezoelektrik özelliklerini incelemek için *Ab initio* hesaplamaları yapılmıştır. Ayrıca, TaS_2 ve türevlerinin elastik ve piezoelektrik özellikleri analiz edilir. TaS_2'nin düzlem içi piezo-elektriğinin bir yüzey florlama ile arttırılabileceği, düzlem dışı simetriye bağlı olarak tüm Janus yapılarına piezoelektriklik için ilave bir serbestlik derecesi eklenebileceği ortaya çıkmıştır. TaS_2'nin tek katmanlı 1H fazının, yüzey işlevelleştirilmesi için uygun bir malzeme olduğunu ortaya koymuştur; böylelikle oluşturulan dinamik olarak kararlı Janus yapıları, piezoelektrik uygulamalar için farklı elektronik özellikler ve ilave serbestlik derecesi gösterir.

Bu tez, kalınlık ve işlevselliğe bağlı mekaniğin anlaşılması, 2D malzemelerin titreşimsel, elektronik özellikleri hakkında bazı önemli sonuçlar vermektedir.

... to my father ...

TABLE OF CONTENTS

LIST OF FIGURES

CHAPTER 1

INTRODUCTION

Layered materials stacked with weak out-of-plane van der Waals (vdW) interaction, have aroused considerable interest for many decades.(Brodie, 1859; Schuller, 1980) In addition, advances in synthesis techniques of layered two dimensional (2D) materials also lead to emergence of variety of monolayer crystals such as graphene,(Novoselov *et al.*, 2004) transition metal dichalcogenides (TMDs),(Geim and Grigorieva, 2013) post-transition metal chalcogenides (PTMCs),(Late *et al.*, 2012) h-BN,(Joshi *et al.*, 2013; Kim *et al.*, 2011) h-AlN,(Zhuang and Hennig, 2012) silicene (Vogt *et al.*, 2012; Cahangirov *et al.*, 2009) and metal hydroxides.

Interest in the field of two dimensional (2D) single-layer materials triggered by the synthesis of graphene (Novoselov *et al.*, 2004) has also led to emergence of novel ultra-thin materials exhibiting remarkable optical, electronic and mechanical properties.(Mas-Balleste *et al.*, 2011; Wang *et al.*, 2012; Kim *et al.*, 2011) Apart from one-atom-thick graphene, single-layers of transition metal dichalcogenides (TMDs) such as MoS_2, $MoSe_2$, WS_2 and WSe_2 have also been added to the library of 2D crystals.(Mak *et al.*, 2010; Ramakrishna Matte *et al.*, 2010; Lee *et al.*, 2010; Splendiani *et al.*, 2010; Coleman *et al.*, 2011; Ataca *et al.*, 2012; Yin *et al.*, 2011; Chhowalla *et al.*, 2013; Zhang *et al.*, 2014; Lu *et al.*, 2014; Huo *et al.*, 2014; Chernikov *et al.*, 2015; Koperski *et al.*, 2015; Nasr Esfahani *et al.*, 2015; Island *et al.*, 2016; Chuang *et al.*, 2016)

In the family of 2D materials, TMDs are desirable both for fundamental research and technological advancement thanks to their interesting optical, electrical properties, and mechanical stability.(Akbali *et al.*, 2017; Ataca *et al.*, 2011; Chhowalla *et al.*, 2013; Mak *et al.*, 2010; Zhang *et al.*, 2014; Castellanos-Gomez *et al.*, 2012) Dichalcogenides of Mo and W, the most popular materials among TMDs, have received considerable interest due to their exceptional physical properties such as ≈ 250 cm^2 V^{-1} s^{-1} room temperature mobility, excellent on/off ratio ($\sim 10^8$), thickness dependent metallic and semiconducting behavior, tunable band gaps, and controllable topological electronic properties.(Wang *et al.*, 2012; Jariwala *et al.*, 2014; Tan and Zhang, 2015; Late *et al.*, 2012; Qian *et al.*, 2014)

Among TMDs, bulk platinum dichalcogenides (PtX$_2$, where X=S, Se, Te) were quite demanded materials owing to their properties such as complete renewability,(Soled

et al., 1976) enhanced adhesion,(Soled *et al.*, 1976) semi-metallic electronic structure,(Guo and Liang, 1986; Kliche, 1985) high optoelectronic efficiency,(Yeo *et al.*, 2002) and enhanced photo- and electro-catalytic behavior.(Chia *et al.*, 2016; Lu *et al.*, 2016) However, recently, 2D single-layer crystals of $PtSe_2$, with high structural stability in air and high photo-responsivity(Zhao *et al.*, 2017; Wang *et al.*, 2015; Yim *et al.*, 2016), has been successfully synthesized by direct selenization of the Pt(111) substrate.(Sajjad *et al.*, 2018) In addition, theoretical studies revealed that single-layer PtS_2 ($PtSe_2$) is a semiconductor with a bandgap of 1.6 eV(Zhao *et al.*, 2016) (1.2 eV(Wang *et al.*, 2015)) having the potential for solar energy harvesting.

Among TMDs, apart from well-known Mo and W dichalcogenides, lamellar crystals of Pt dichalcogenides have also attracted interest due to their semi-metallic electronic structure,(Guo and Liang, 1986; Kliche, 1985) high optoelectronic performance,(Yeo *et al.*, 2002) and enhanced photocatalytic activities.(Ullah *et al.*, 2014; Ye and Oh, 2016) Besides their bulk form, 2D Pt dichalcogenides suggest promising materials for nanoelectronic device applications due to their intriguing electronic properties such as transition from metal to semiconductor.(Wang *et al.*, 2015; Zhao *et al.*, 2016; Du *et al.*, 2018) It was shown that few-layer PtS_2 phototransistor exhibits a very high responsivity reaching 1.56 x 10^3 A W^{-1}.(Li *et al.*, 2017) In addition, Zhao *et al.* reported that few-layer $PtSe_2$ field effect transistor (FET) exhibits high electron mobility at room-temperature ($\approx$210 cm^2 V^{-1} s^{-1}) on SiO_2/Si substrate.(Zhao *et al.*, 2017) Chia *et al.* investigated the correlation between varying chalcogen type to the electrochemical and catalytic performances of Pt dichalcogenides.(Chia *et al.*, 2016) Very recently, it was revealed that vertically aligned $PtSe_2$/GaAs heterojunction shows broad sensitivity to illumination ranging from deep ultraviolet (UV) to near-infrared (NIR) light.(Zeng *et al.*, 2018) Similarly it was shown that multilayer $PtSe_2$/$FA_{0.85}Cs_{0.15}PbI_3$ perovskite heterojunction photodetectors are ultrafast, self-driven and air-stable and also exhibited high sensitivity to illumination range from the UV to NIR spectrum region(Zhang *et al.*, 2018). Sattar *et al.* reported that monolayer and bilayer $PtSe_2$ form n-type and p-type Schottky contact with graphene, respectively. Sajjad *et al.* demonstrated that monolayer 1T-$PtSe_2$ is a good candidate for gas sensor applications due to high adsorption energy and robust character of the band edges of electronic band structure.(Sajjad *et al.*, 2017) Furthermore, Yao *et al.* investigated that centrosymmetric monolayer $PtSe_2$ thin film exhibits R-2 Rashba effect and intrinsic spin-layer locking.(Yao *et al.*, 2017) In the very recent study Ciarrocchi *et al.* showed that high electrical conductivity and efficient transistor operation can be achieved by using only $PtSe_2$ material by varying the thickness from 14 to 2 nm.(Ciarrocchi *et al.*, 2018)

Recently, various techniques such as the construction of both vertical and lateral heterostructures have been applied to 2D materials in order to combine their different properties in a material.(Ben-Melech Stan and Caspary Toroker, 2018; Woods *et al.*, 2016) Although, such combination is experimentally feasible, the size and quality of the heterostructure strongly influenced by the synthesis technique which may limit their applications. Moreover, recent studies have revealed that the synthesis of Janus type 2D materials can be an efficient way to enrich the functionality of a 2D crystal since different monolayers can be combined in a single-layer with strong chemical bondings.(Lu *et al.*, 2017) The fact that the two surfaces of Janus materials have different properties inspired the development of nanodevices in the fields of chemistry, biology, and physics.(Zhang *et al.*, 2017; Zhao and Pumera, 2014; Wu *et al.*, 2014; Ma *et al.*, 2014) Furthermore, recent theoretical studies have reported the energetic feasibility of Janus type single-layer crystals such as In_2SSe,(Kandemir and Sahin, 2018) $MoSe_2$,(Zhang *et al.*, 2017) MXY (M = Mo,W and X/Y = S, Se, Te).(Cheng *et al.*, 2013; Dong *et al.*, 2017) It was shown that intrinsic out-of-plane electric field induced in single-layer Janus crystal leads to significant Rashba spin splitting in electronic band dispersion of WSeTe.(Cheng *et al.*, 2013) In addition, synthetically-synthesized Janus single-layer of TMDs have found to be displaying higher piezoelectric performance than commonly used materials.(Dong *et al.*, 2017)

Among TMCs, TaS_2 has attracted great attention and has been extensively due to its superconducting state. In addition, TaS_2 has four different phases over a wide temperature range, from 77 to $400\,^\circ K$.(Geremew *et al.*, 2019) TaS_2 is a layered material and TaS_2 is the only transitional metal dichalcogenide (TMD) known to have formed the Mott phase. In a developed ionic effect transistor Li-ion interference has been reported to modulate the properties of TaS_2. Strong charge doping induced by adjustable ion intercalation changes the energy of the various charge sequence states in TaS_2 and produces a series of phase transitions in dimensionally reduced flake samples.(Yu *et al.*, 2015) In addition, high hydrogen evolution reaction efficiency was obtained for TaS_2, so that TaS_2 was shown to be a pioneer in the discovery of novel, efficient catalysts.(Shi *et al.*, 2017)

However, functionalization of two-dimensional materials in terms of acquiring new properties is very important. It was shown that fluorination in 2D materials can lead to tunable electronic optical and mechanical properties of the material.(Nair *et al.*, 2010; Şahin *et al.*, 2011; Sreepal *et al.*, 2019) In addition, fluorination has been shown to allow a number of potent reaction paths for subsequent chemical modification compared to fluorinated carbon nanotubes.(Wang *et al.*, 2018) Fluorinated graphene has been revealed to be more efficient for oxygen reduction reaction (ORR) catalysts due to its lower overpo-

tential and a good alternative to a metal-free catalyst for the removal of organic pollutants in catalytic ozonation.(Zhao *et al.*, 2016; Li *et al.*, 2015)

Hydrogenation, another important step of the chemical functionalization technique of materials, has been used to investigate possible pathways for potential aplications such as hydrogen storage systems in 2D electronics.(Sofo *et al.*, 2007; Yagmurcukardes *et al.*, 2017) In particular, hydrogenation and fluorination have created a suitable area for band gap engineering. Chemical functionalization creates a tunable band gap in 2D materials, allowing for conductive, flexible, transparent new device structures using the electronic, optical and mechanical properties of the materials.(Fuhrer *et al.*, 2010; Wehling *et al.*, 2008; Robinson *et al.*, 2010)

In addition to research on TMDs, Janus-type 2D materials were obtained, which allows the collection of different layer properties of TMDs in a single polar material in both experimental and theoretical studies.(Lu *et al.*, 2017; Kandemir and Sahin, 2018; Zhang *et al.*, 2017; Cheng *et al.*, 2013; Dong *et al.*, 2017; Kahraman *et al.*, 2019) It was revealed that the intrinsic out-of-plane electric field induced in Janus structures causes Rashba spin splitting in the electronic band distribution and Janus structures have higher piezoelectric properties than TMDs.(Cheng *et al.*, 2013; Dong *et al.*, 2017; Kahraman *et al.*, 2019)

In this study, motivated by the recent studies revealing the superior properties of TaS_2 and inspiring the successfully synthesized hydrogenated, fluorinated and Janus structure, we investigate the structural, vibrational, electronic and piezoelectric properties of TaS_2 and its derivatives.

CHAPTER 2

COMPUTATIONAL METHODOLOGY

2.1. Many-Electron Systems

The interaction of many-electron systems creates some of the most remarkable challenges to understand quantum mechanics in many applications. However, because these systems with quantum mechanical wave functions are difficult to resolve, density functional theory (DFT) has become a useful and popular approach.

DFT is an approach which is popular and powerful in quantum mechanics for determining ground states; electronic, magnetic, optical and mechanical properties interacting with many electron systems, such as solids and molecules used in physics, chemistry and the science of materials. Because of the fact that the wave function is not really observable in quantum mechanics, the ability of DFT to produce very accurate results at low cost means that it is able to describe all materials ' physical ground state properties as to electronic density.

All information about a physical system can be found in a quantum mechanical wave function. The time-dependent Schrodinger equation may constitute the mathematical expression of this wave function.

$$\hat{H}\Psi = E\Psi \tag{2.1}$$

This expression is non-relativistic. $\hat{H}$ is the Hamiltonion operator, Ψ is a set of wave (eigen) functions and E the corresponding eigenvalues. While the Eq 2.1 solves single-electron systems like hydrogen perfectly, It can not be done with perfect precision with Schrodinger Equation for N-electron atomic systems without any approximation.

The Hamiltonian operator provides terms for every possible interaction between electrons and nuclei for a system containing M nuclei and N electrons. The wavefunction of the system as a consequence of this form of $\hat{H}$ is the function of spatial nuclei (R_A,

A=1,...,M) and electron (r_i, i=1,...,N) coordonates.. The $\hat{H}$ operator has the general form for N-body system is

$$\hat{H} = -\sum_{A=1}^{M} \frac{\nabla_A^2}{2M_A} + \sum_{i=1}^{N}\sum_{j>1}^{N} \frac{1}{|\vec{r_i} - \vec{r_j}|} + \sum_{A=1}^{M}\sum_{B>A}^{M} \frac{Z_A Z_B}{|\vec{r_i} - \vec{r_j}|} - \sum_{i=1}^{N}\sum_{A=1}^{M} \frac{Z_A}{|\vec{r_i} - \vec{R_A}|} \quad (2.2)$$

All terms describing all possible interactions of N-electron quantum mechanical system are found in this Hamiltonian operator. The first two terms are the electrons and nuclei's kinetic terms of energy. M_A is the ratio of the mass of the nucleus to that of the electron in the second term and Z_A is the nucleus number. In the electron and nucleus coordinates the ∇_i^2 and ∇_A^2 are laplacian operators, respectively. The third and fourth terms are the Coulomb repulsion terms, respectively, between electrons and nuclei and the last term is the interaction of the Coulombic electron with the nucleus. While the Schrodinger equation for this Hamiltonian is written easily by hand, it does seem impossible. Many approaches were therefore proposed to simplify the answer for this $\hat{H}$.

2.1.1. Born-Oppenheimer Approximation

Born-Oppenheimer approximation, which Max Born and J formed Robert Oppenheimer thought that the nuclei were much heighter than the mass electrons in 1927. Thus, nuclei can be viewed with regards to electrons as static, classic particles. The kinetic term of nuclei can therefore be removed in Eq. 2.2 whereas in the fourth term the fixed nuclei configuration makes a constant. Hamiltonyen becomes known as electronic Hamiltonyen with three terms left,

$$\hat{H}_e = -\sum_{i=1}^{N} \frac{\nabla_i^2}{2} + \sum_{i=1}^{N}\sum_{j>1}^{N} \frac{1}{|\vec{r_i} - \vec{r_j}|} - \sum_{i=1}^{N}\sum_{A=1}^{M} \frac{Z_A}{|\vec{r_i} - \vec{R_A}|}. \quad (2.3)$$

Following this simple assumption, this Hamiltonian wavefunction is only the function of the electron position r_i. Under the approximations of Born-Oppenheimer, the corresponding Schrodinger equation appears to be simpler than its most generally acceptable form. (Eq. 2.4)

$$\hat{H}_e \Psi_e(r_i) = E_e \Psi_e(r_i) \tag{2.4}$$

Although it seems to be a simple form, the term interaction between electron and electron is in Eq. 2.3 because the movement of electrons is interrelated. The instantaneous coordinates of each electron, which basically require 3^N variables for the N-electron system, should also be considered. Different approximations were established for Schrodinger's solution of N-interacting electrons. The aim of these approximations is to map Schrodinger N-electron into an suitable Schrodinger equation with one-electron. DFT in which the electron density is regarded central quantity is one of these approximation methods.

2.1.2. Thomas-Fermi Model

Thomas and Fermi first proposed the idea that electronic energy could be expressed in terms of electron density in the 1920s (Thomas, 1927; Fermi, 1927). The Thomas-Fermi theory presupposes that interactions between electron-nucleus and electron-electron are classical and the electron's kinetic energy is computed only as a functional element of electron density. Non-interacting electrons are acceptable within a homogenous electron density. The term of kinetic energy can be used as electron density functional, where the Fermi CF coefficient in atomic units equals 2.781.

$$T[n] = C_F \int n^{5/3}(\mathbf{r})dr \tag{2.5}$$

The total system energy in electron-density consists of the two interaction terms, electron-electron and electron-nucleus, which include the second and third term electron-nucleus and the electron-electron interaction terms.

$$E[n] = C_F \int n^{5/3}(\mathbf{r})dr - Z \int \frac{n(\mathbf{r})}{r}dr + \frac{1}{2} \int \int \frac{n(\mathbf{r_1})n(\mathbf{r_2})}{|r_1 - r_2|}dr_1 dr_2 \tag{2.6}$$

And after that, when this total energy functions are known, the system's ground-state energy can be determined by minimizing the functional, E[n], for every possible electron density, n(r) to fulfill.

$$N = \int n(\mathbf{r}) d^3 r \qquad (2.7)$$

Instead of the ground state energy performance, the main purpose of the Thomas-Fermi model is to demonstrate that total energy can be examined by means of electron density.

2.2. Density Functional Theory

The Schrodinger equation can be solved by direct approximation of the wave functions of Ψ. However, even for the small system, the difficulty of the solution expands exponentially with the number of electrons. The density functional theory uses the electron density (n(r)) that is simpler rather than the complex N electron wave function of Ψ and Schrodinger equation. Regardless of the total electrons that deal in the system, the density is lowered from 3N to 3, as n(r) always has three degrees of liberty. This decrease in degree of total freedom allows DFT to be applied easily to a larger system.

The electron density is first and foremost described as,

$$n(r) = N \int ... \int |\Psi(r_1, r_2, ..., r_N)|^2 dr_1, dr_2, ..., dr_{N-1} \qquad (2.8)$$

Where the N-1 electrons are arbitrarily placed, and n (r) defines the possibility of finding any one of the N electrons. Moreover, Ψ (r_1, r_2,..., r_N) is the Schrodinger equation solution and depends on each electron's position. Now some electron density models in DFT are debated.

2.2.1. Hohenberg-Kohn Theorems

Hohenberg and Kohn initiated the approach in 1964. They showed that DFT can be regarded as a special functional density that applies to the ground states of a quantum

many-body system that an exact theory enabling one to identify the electronic Hamiltonian as an electron density functional, n(r). Two major theorems are found in this model; (i) The external potential,$Vext$, (and therefore total energy) is a function of the electron density that is unique. When two electric systems, one in a potential v_1 and one in v_2 trapped, have the same density n of the ground-state , then v_1 -v_2 is necessarily stationary. The density of the ground state determines the system's potential and therefore all its properties, including the many-body wavefunction. (ii) The functionality provides the system's energy in the ground state on only when the input density is the true ground state density. The energy is the minimum energy. The density of electron n_0(r) of the ground state can be determined with a principle of variation. Then the total energy functional for a particular $Vext$ becomes as,

$$E = \frac{\langle \Psi_0 \left| H \right| \Psi_0 \rangle}{\langle \Psi_0 | \Psi_0 \rangle} \equiv \langle H \rangle = \langle T \rangle + \int d^3\mathbf{r} V_{ext}(\mathbf{r}) n_0(\mathbf{r}) + \langle V_{int} \rangle + E_{II} \qquad (2.9)$$

2.2.2. Hellmann-Feynman Theorem

The theorem have been proven independently by Hellmann and Feynman in 1930s. In the Hellmann-Feynman theorem, quantum mechanics refers to the derivative of total energy in relation to a parameter and to the Hamiltonian derivative's expectation value for that parameter. According to the theorem, expectation value of the Hamiltonian depends on nuclear positions, because the Hamiltonian molecular depends on its external potential,$Vext$, and implicitly, on the ground-state wave function that depends on nuclear coordinates,so all the forces of the system can be calculated by using classical electrostatics when spatial distribution of electrons are defined through the solution of the Schrodinger equation.

$$\mathbf{F}_I = -\frac{\partial E}{\partial \mathbf{R}_I} \qquad (2.10)$$

Only electron density, n and the other nuclei are responsible for the force. If the definition of total energy in equation 2.9 is written in the the force can be found as follows,

$$\mathbf{F}_I = -\frac{\partial E}{\partial \mathbf{R}_I} = -\int d^3 \mathbf{r} n(\mathbf{r}) \frac{\partial V_{ext}(\mathbf{r})}{\partial \mathbf{R}_I} - \frac{\partial E_{II}}{\partial \mathbf{R}_I} \qquad (2.11)$$

2.2.3. The Kohn-Sham Equations

Kohn and Sham develop a model that can transform DFT into a practical electronic structure theory in 1965. Although it has been proven by Hohenberg-Kohn to use the basic the ground state density to calculate the properties of the system, this does not provide a solution to find the the ground state density. The Kohn-Sham equations are a route to this. In order to derive these equations, it takes into account the ground state energy given as a functionality of the ground state density. The functional energy in Eq. 2.12 becomes as the following form,

$$E[n] = \int F_{HK}[n] + n(r)V_{ext}(r)dr = \int n(r)V_{ext}(r)dr + T[n] + E^{Hartree}[n] + E_{xc}[n]$$
$$(2.12)$$

The first term, $F_{HK}[n]$, in equation is the sum of kinetic energy of non-interacting electrons that contain T[n], Hartree energy, $E^{Hartree}$ and exchange and correlation energy, E_{xc}. The crucial step here is to describe a effective potential, as defined,

$$V^{eff} = \frac{\delta\{\int n(r)V_{ext}(r)dr + E^{Hartree}[n] + E_{xc}[n]\}}{\delta n(r)}, \qquad (2.13)$$

which leads to the following equation.

$$V^{eff} = V_{ext}(r) + \int \frac{n(r')}{|r - r'|}dr' + V_{xc}(r), \qquad (2.14)$$

V_{xc}(r) is the exchange-correlation potential calculated from the exchange-correlation energy. Using the potential here, In the case of Kohn-Sham DFT, the Schrodinger equation uses the potential as an electron-like equation known as the one-electron orbitals of Khon-Sham, whose eigenfunctions give rise to the electron density of ϕ_i.

$$\left[-\frac{1}{2}\nabla^2 + V^{eff}\right]\phi_i = E_i\phi_i \tag{2.15}$$

$$n(r) = \sum_{i=1}^{N} |\phi_i|^2 \tag{2.16}$$

According to the Eq. 2.16, effective potential, V_{eff} is density, n(r), dependent. To solve the khon-sham equations, the following path can be followed; (i) estimation of electron density, (ii) finding effective potential,V^{eff}, using electron density information, (iii) calculating the corresponding khon-sham orbitals,ϕ_i, (iv) the calculation and comparison by the first state of the new electro density corresponding to these pathways. When convergence is achieved, the total energy can be calculated from the final state of electron density. Although the last electron density has been figured, the exchange-correlation energy has not yet been found.

2.2.4. The Types of Exchange-Correlation Functionals

Only non-interacting parts of energies can be calculated with the Kohn-Sham equation in DFT. Pauli is defined by the principle of exclusion as one of the energy terms is the energy of change from a fermionic wave function with an antisymmetric structure. The other energy terms are due to the effects of the electron correlation on kinetic and potential energy. In other words, the exchange-correlation energy can be defined as the difference between the total energy in a quantum mechanical system and the Hartee energy. In addition the exchange-change correlation energy should include a term to regulate the interaction of the electron density with itself. In order to complete the Kohn-Sham equations, different approaches have been developed for the E_{xc} term, the most common ones are generalized gradient approximation (GGA) and local density approximation (LDA) in DFT based calculations.

2.2.4.1. Local Density Approximation (LDA)

The simplest approximation is to assume that the energy density of the exchange-correlation is identical to that found for the uniform electrons in each position in the space of the molecule. This approach, originally developed by Perdew and Zunger(Perdew and Zunger, 1981), has a slowly varying electron density. The exchange-correlation energy obtained using this approach is as follows:

$$E_{xc}^{LDA}[n] = \int n(r)\epsilon_{xc}^{unif}[n]dr \qquad (2.17)$$

ϵ_{xc}^{unif} is the exchange-correlation energy per electron of a uniform electron gas density. LDA is a well-working approach, especially in metallic systems. When the cohessive energies are calculated very well, lattice parameters cannot be calculated with the same precision.

2.2.4.2. Generalized Gradient Approximation (GGA)

LDA approaches the density almost as constant as it finds the energy of the actual density, so this approach fails because the density changes rapidly in structures such as molecules. A development with Generalized Gradient Approximation (GGA) can be achieved to eliminate this problem; this approach takes into account the gradient of electron density. To find the total energy that is functional in the GGA, the electron density and its gradient should contain in the formula,

$$E_{xc}^{GGA}[n] = \int f^{GGA}(n(r), \nabla n(r))dr \qquad (2.18)$$

GGA approximation is also known as semi-local functionals because of their gradient of the electron density. Compared to LDA, GGA has been found to provide more successful results in the geometry and ground state energy calculations.

2.3. Theory of Phonon

Phonons which play a significant role in different solid state phenomena are quanta of lattice vibrations. To find the stability of a material in equilibrium or under stress, it is necessary to calculate the phonon band distribution along Brillouin Zone. In theory, at an absolute zero temperature, the atoms of a crystal are at their lowest energy position without any movement. When thermal energy is added to the crystal, this balance location is expressed through vibration of the atoms. The electric forces which bind atoms together stretch or compress a little to a higher energy configuration within the limits of fairly small vibrations. Each nuclear acts as if it is connected by small springs with its neighbours. The added energy is stored in the crystal as the kinetic energy of the moving atoms and the potential energy of the compressed or stretched springs. This theorem, also known as hooke law, is formalized as follows;

$$F = -kX, \tag{2.19}$$

In the formula x is the distance between the masses, k is the spring constant. In this section introduces the methodology of calculating phonon band distributions in DFT. As mentioned above, it is necessary to replace the atoms in order to find the phonon distributions of a material, and there must be matrix representations of force constants. A small displacement method must be used to achieve this. In order to use this methodology, the unit cell within the crystal must first be transformed into a super cell of sufficient size. Each atom contained in the super cell generated should be placed along cartesian coordinates, there will be a displacement amount resulting from harmonic movement and also the amount of displacement can be reduced by using symmetry in the crystal. The resulting Hellmann-Feynman forces are calculated for each of these displacements and the dynamic matrix is built. At low temperatures the potential energy of crystalline is as follows:

$$U_{harm} = E_{eq} + \frac{1}{2} \sum_{ls\alpha,l't\beta} \Phi_{ls\alpha,l't\beta} u_{ls\alpha} u_{l't\beta}, \tag{2.20}$$

Where E_{eq} is crystal energy at ion equilibrium positions, whereas x refers to a movement of the atom s^{th} in cell unit l along α or β cartesian directions.The term $\Phi_{ls\alpha,l't\beta}$

in the formula is the force-constant matrix, the second derivative of the harmonic potential energy for displacing. The relationship among the forces in each atom, F_{ls}, and the shifts , u_{ls},, which should be linearly related, can be found if the harmonic energy given in Eq. 2.20 is differentiated.

$$F_{ls\alpha} = -\sum_{l't\beta} \Phi_{ls\alpha,l't\beta} u_{l't\beta}, \qquad (2.21)$$

If the force matrix, $\Phi_{ls\alpha,l't\beta}$, are found first, the dynamic matrix can be easily identified as follows;

$$D_{s\alpha,t\beta} = \frac{1}{\sqrt{M_s M_t}} \sum_l e^{i\mathbf{q}(R_{l't\beta} - R_{ls\alpha})} \Phi_{ls\alpha,l't\beta}, \qquad (2.22)$$

The terms M_s and M_t in the formula are the masses of the sth and l^{th} atoms, respectively. In the cartesian components α and β the term on the exponential function, $R_{l't\beta} - R_{ls\alpha}$, represents the distortion of atoms.

When the matrix is found, the the eigenvalue equation of the force-constant matrix of its value can be solved. give the allowed (squares of) phonon frequencies for a given The eigenvalues of the dynamical matrix values provide the allowed (squares of) phonon frequencies for a given on every wave vector,q, in every phonon branch for the crystal. The total number of branches of the phonon gives the total number of degrees offreedom phonons the crystal. The size of dynamical matrix also depends on the number of phonon branches. In the unit cell, there are 3*N* phonon branches in a crystal structure containing N atoms and 3 of them are acoustic and 3*N*-3 are optical. PHONOPY (Togo *et al.*, 2008) was used to calculate the phonon distributions of the materials made throughout this thesis. This code makes use of the Hellmann-Feynman forces to calculate phonon distributions by the software Vienna *Ab-initio* Simulation Package (VASP) (Kresse and Furthmuller, 1996) which is based on DFT.

2.4. Heterostructures and Band Alignments

Energy bands of two distinct materials come together at heterojunctions of semi-conductors, leading to an interaction. Both band structures are placed discontinuously to

align near the interface. It is reason that throughout the two semiconductors, the Fermi energy level remains continuous. This relative alignment of the bands of energy of the semiconductor is called the band alignment. Two types of interface variables, the band discontinuities and the built-in potential determine the band alignments. These discontinuities are triggered by the difference in semiconductor band gaps and are divided between two discontinuities of the band, the valence band, and conduction band. The built-in potential is triggered by the bands that bend close to the interface owing to a load imbalance between the two semiconductors.

The behavior of heterostructures of semiconductors depends on the alignment at the interface of the energy bands and thus on the alignments of the bands. Such heterostructures interfaces can be classified into three kinds: straddling gap (known as type-I), staggered gap (known as type-II), and broken gap (known as type-III). In a type-I heterostructure, the relationship between the conduction band minimum (CBM) and the valence band maximum (VBM) between the composite layers A and B should be as follows: $VBM_B < VBM_A < CBM_A < CBM_B$. thus, since the conduction band minimum (CBM) and the valence band maximum (VBM) are placed in a layer, it is seen that the electrons and holes are recombination more efficiently when stimulated by light. For type-II heterostructure, the rule is as follows, $VBM_A < VBM_B < CBM_A < CBM_B$. Therefore, in these structures CBM and VBM are in different layers. At the interface, electron-hole pairs can be divided, electrons transmitted to one layer and holes transmitted to the other. On the other hand, the CBM and the VBM of two composite layers (A and B) follow the following rule in a type-III heterostructure: $VBM_A < CBM_A < VBM_B < CBM_B$.

2.5. Computational Methodology

Density functional theory (DFT) calculations were performed using the Vienna *ab-initio* Simulation Package (VASP) (Kresse and Hafner, 1993; Kresse and Furthmuller, 1996). The Perdew-Burke-Ernzerhof (PBE) (Perdew *et al.*, 1996) form of generalized gradient approximation (GGA) was adopted to describe electron exchange and correlation. The van der Waals (vdW) correction to the PBE functional was done using the density functional theory long-range dispersion correction (DFT-D2) method of Grimme (Grimme, 2006).

In this thesis writing, the same parameters were taken with different values and calculations were made using the same methods. The methodology for the third part is as follows. The kinetic energy cutoff for a plane-wave basis set was taken 500 eV. The

convergence criterion of self-consistent calculations for ionic relaxations was 10^{-6} eV between two consecutive steps and the total force of the all atoms in the unitcell was reduced to a value of less than 10^{-5} eV/Å. Pressures on the used lattice unit cells were decreased to values less than 1.0 kbar. To hinder interactions between the adjacent cells along the *z*-direction, at least 14 Å vacuum space was used.

The methodology used in the fourth chapter is as follows: The kinetic energy cutoff for a plane-wave basis was set to 400 eV. For the convergence criterion of self-consistent calculations in ionic relaxations, the total energy difference between the consecutive steps was taken to be 10^{-6} eV. The total force on the atoms in the primitive unit-cell was reduced to a value of less than 10^{-5} eV/Å while the pressures on the lattice were decreased to values less than 1.0 kbar in all directions. To eliminate interaction between the adjacent layers, at least 18 Å of vacuum space was inserted. For the band alignment calculations, the dipole corrections were taken into account in order to compensate the effect of induced out-of-plane dipole moment in Janus structures.

Analysis of the charge transfers in the structures was determined by using Bader technique. (Henkelman *et al.*, 2006) To hinder interactions between the adjacent cells along the *z*-direction, at least 14 Å vacuum space was used.The cohesive energy per formula E_{Coh} was calculated by using the formula as $E_{Coh} = [n_1 E_1 + n_2 E_2 - E_{ML}]/n_{tot}$, where E_1 and E_2 represent the energies of single isolated two atoms, respectively. E_{ML} stands for the total energy of the 1T-PtX$_2$ structure, n_{tot}, n_1 and n_2 denote the total number of atoms, number of Pt and X atoms within the unitcell, respectively. The vibrational properties were calculated with PHONOPY code (Togo *et al.*, 2008) that uses finite-displacement method. Phonon eigenfrequencies in whole Brillouin Zone (BZ) and phonon eigenvectors were calculated in a 75-atom supercell.

The methodology used in the fifth chapter is as follows: All calculations were performed by using density functional theory (DFT) with generalized gradient approximation (GGA) as implemented in the Vienna *ab-initio* Simulation Package (VASP).(Kresse and Furthmuller, 1996; Kresse and Hafner, 1993) The Perdew-Burke-Ernzerhof (PBE)(Perdew *et al.*, 1996) was adopted to describe electron exchange and correlation. To describe the interaction of the long-range van der Waals (vdW), the dispersion interactions were calculated from the empirical pair corrections implemented by using Grimme(Grimme, 2006) in the DFT-D2 method.

For all calculations, a plane-wave basis set with a kinetic energy cutoff was taken as 500 eV. While the convergence criterion of the total force on the atoms in the primitive unitcell was set to 10^{-5} eV/Å, the energy convergence criterion was set to 10^{-6} eV and

the pressures on the lattice have been reduced in all directions to values less than 1.0 kbar. A vacuum space of at least 20 Å was used to eliminate interaction between the adjacent layers. Bader(Henkelman *et al.*, 2006) technique was used to determine analyses of the charge transfers in the structures.

The cohesive energy per formula was calculated by using the formula,

$E_{Coh} = [\sum n_{atom} E_{atom} - E_{ML}]/n_{tot}$, where E$_{atom}$ represents the energy of single isolated atom. E$_{ML}$ is the total energy of the structure, n_{tot}, n_{atom} denote the total number of atoms, the number of atom within the unitcell, respectively. The dynamical stability of all structures were evaluated by calculating their phonon band dispersion using the PHONOPY code(Togo *et al.*, 2008) which uses finite-displacement method, eigenfrequencies at high symmetry points of the Brillouin Zone (BZ).

CHAPTER 3

PROPERTIES OF PtSe$_2$: FROM MONOLAYER TO BULK

3.1. Structural Properties

For a complete analysis how structural, electronic and phononic properties of the PtSe$_2$ crystal evolve with the thickness, we first investigate characteristics of monolayers comprehensively. The optimized atomic structure of the octahedral coordination forming 1T polytype of PtSe$_2$ belongs to P$\bar{3}$m1 space group. As shown in Fig. 3.1(a), the Bravais lattice of 1T-PtSe$_2$ monolayer is hexagonal with lattice vectors, $\overrightarrow{a} = 0.5a(\sqrt{3}\widehat{x} - \widehat{y})$, $\overrightarrow{b} = 0.5a(\sqrt{3}\widehat{x} + \widehat{y})$, $\overrightarrow{c} = c\widehat{z}$. 1T-PtSe$_2$ structure with D$_{3d}$ point group symmetry is composed of three atomic sub-layers with Pt layer sandwiched between two Se layers. The lattice constant of the primitive unit cell of the monolayer 1T-PtSe$_2$ structure is calculated to be 3.70 Å which is in perfect agreement with previously reported scanning transmission electron microscopy (STEM) data.(Wang *et al.*, 2015) The Pt-Se bond length in the 1T phase of PtSe$_2$ crystal structure is found to be 2.52 Å. Moreover, the thickness, defined as vertical distance between uppermost and lowermost Se layers, of 1T-PtSe$_2$ monolayer is (2.68 Å) is also close to the reported value of 2.53 Å.(Wang *et al.*, 2015) It is also found that the monolayer 1T-PtSe$_2$ is formed by a cohesive energy of 4.43 eV/atom which is comparable to the cohesive energy of MoSe$_2$ and WSe$_2$ ($\sim$ 4.56 and $\sim$ 5.15 eV/atom, respectively).(Lee *et al.*, 2017) According to Bader charge analysis, there is no net charge transfer between bonded atoms in monolayer 1T-PtSe$_2$ structure and the bond character is entirely covalent in monolayer 1T-PtSe$_2$ structure. In addition, the work function is obtained as 5.36 eV in the monolayer 1T-PtSe$_2$ which is higher than that of similar dichalcogenides such as MoSe$_2$ and WSe$_2$ (4.57 and 4.21 eV, respectively)(Gong *et al.*, 2013).

However, structures obtained from total energy optimization calculations may not correspond to the ground state structure, therefore; for a reliable analysis on the stability of a structure it is also necessary to examine the dynamical stability via phonon calculations. The phonon dispersion curves of the 1T-PtSe$_2$ crystal structure are shown in Fig. 3.1(b).

For the primitive unit cell of 1T-PtSe$_2$ composed of 3 atoms, phonon spectrum includes 9 phonon, 3 acoustic and 6 optical, branches, Analysis of lattice dynamics shows
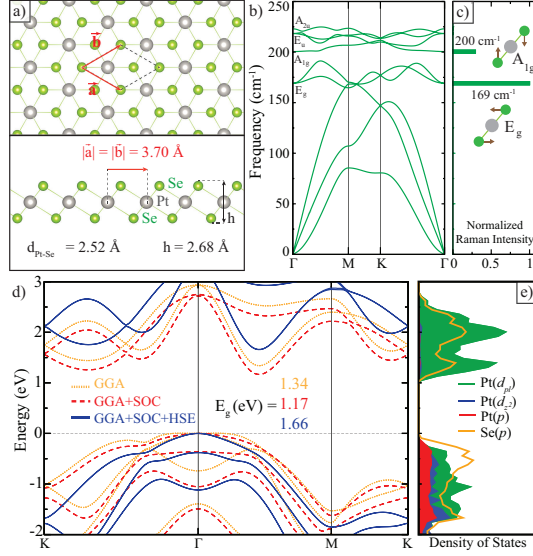
Figure 3.1. Geometric, vibrational, electronic diagrams of 1T-PtSe$_2$ mono-
layer,respectively. The Fermi level is set to zero.

that the decomposition of the vibration representation of optical modes at the Γ point is
$\Gamma=2E_g+2E_u+A_{1g}+A_{2u}$ for the 1T-PtSe$_2$ monolayer structure. Optical phonons include
two doubly degenerate in-plane vibrational modes at 169 cm^{-1} (E$_g$) and 218 cm^{-1} (E$_u$),
and two singly degenerate out-of-plane vibrational modes at 200 cm^{-1} (A$_{1g}$) and 223
cm^{-1} (A$_{2u}$). Vibrational spectrum with eigenfrequencies through whole the Brillouin
Zone indicate that of the 1T-PtSe$_2$ phase corresponds to a dynamically stable crystal struc-
ture. Besides, due to atomic mass and bonding type of Pt and Se atoms, the phonon modes
of 1T-PtSe$_2$ lie at much lower energies when compared to those of well-known 2D tran-
sition metal diselenides, MoSe$_2$ and WSe$_2$.(Qian *et al.*, 2014)

Regarding Raman intensities, in the vibrational spectrum of 1T-PtSe$_2$, there are
two prominent peaks likely to be observed in experiments. As shown in Fig. 3.1(c),
(i) one highly intense in-plane E$_g$ mode at 169 cm^{-1} and (ii) one moderate intense out-
of-plane A$_{1g}$ mode at 200 cm^{-1}. Due to strong covalent character between Pt and Se
atoms, out-of-plane motion of the Se atoms has less contribution in the Raman intensity
compared to in-plane motion of the Se atoms. Corresponding eigenvectors of the Raman
active E$_g$ and A$_{1g}$ modes are also sketched in Fig. 3.1(c).

As shown in Fig.3.1(d), 1T-PtSe$_2$ monolayer is an indirect band gap semicon-
ductor with its valence band maximum (VBM) residing at Γ point and conduction band
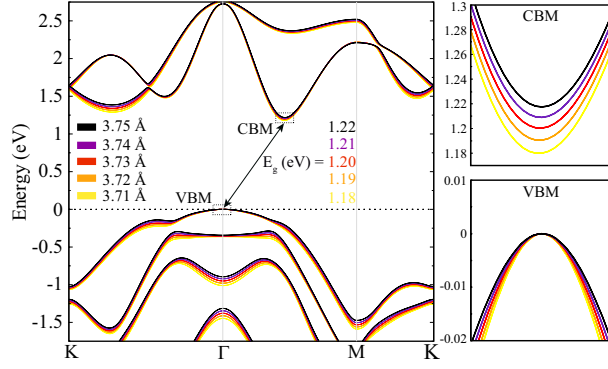
Figure 3.2. The SOC included electronic band diagrams of 1T-PtSe$_2$ monolayer as a function of tensile biaxial strain

minimum (CBM) within Γ-M point. Calculations with, without spin-orbit interactions and HSE correction show that the band gaps of 1T-PtSe$_2$ monolayer are 1.34, 1.17 and 1.66 eV, besides; no change is seen at the band edges of CBM and VBM. With the effect of spin-orbit coupling (SOC), double degenerate VBM is separated at Γ point about 0.4 eV in the 1T-PtSe$_2$ monolayer and also CBM splits 170 meV at the point between Γ and M. It is seen that HSE correction increases the band gap about 0.5 eV.

As seen in Fig.3.1(e), calculated orbital projected partial density of states (PDOS) reveals that the valence states are mainly composed of hybridization of d and p orbitals of Pt, and p orbitals of Se atoms. However, the conduction states consist of d_{xy}, d_{yz}, d_{xz} and $d_{x^2-y^2}$ orbitals (d_{pl}) of Pt atom and p orbital of Se atoms. In addition, PDOS shows that d and p orbitals of Pt, and p orbitals of Se are responsible for the VBM of the monolayer, whereas only d_{xy}, d_{yz}, d_{xz} and $d_{x^2-y^2}$ orbitals (d_{pl}) of Pt are dominantly responsible for CBM of the 1T-PtSe$_2$ structure.

Since the effect of strain due the adjacent layers is inevitable in such lamellar crystal structures, before studying the thickness dependent properties, we investigate electronic and structural parameters under biaxial strain. Here we apply the strain by scanning the lattice parameters in between monolayer and bulk 1T-PtSe$_2$. It is found that the Pt-Se bond length monotonically increases, while tensile strain rate increases. As seen from Fig.3.2, while VBM at the Γ point is quite insensitive against the biaxial strain, CBM at the Γ-M symmetry point shifts upwards slightly in the energy space. Hence, the reasonable tensile strain causes to change slightly the electronic band gap of the monolayer 1T-PtSe$_2$ structure. Against tensile deformation, the 1T-PtSe$_2$ monolayer is the quite robust

Table 3.1. The calculated parameters for the 1T-PtSe$_2$ structures are; the lattice constants, $a=b$; overall thickness as the uppermost-lowermost Se-Se distance in the unitcell, h; the charge donation from Pt to Se atoms, $\Delta\rho$; the cohesive energy per atom, E$_{Coh}$; Φ and μ are the values of work function and magnetization, respectively; E$_{gap}$, the energy band gap of the structure.

	$a=b$ (Å)	h (Å/unitcell)	$\Delta\rho$ (e^-)	E$_{Coh}$ (eV/atom)	Φ (eV)	μ (μ_B)	E$_{gap}$ (eV)
1L PtSe$_2$	3.70	2.68	0	4.43	5.36	0	1.17
2L PtSe$_2$	3.73	7.39	0	4.53	4.64	0	0.19
3L PtSe$_2$	3.74	12.04	0	4.57	4.67	0	0
4L PtSe$_2$	3.75	16.67	0	4.59	4.72	0	0
Bulk PtSe$_2$	3.77	2.56	0	4.65	4.76	0	0

semiconductor material which is the essential factor for its utilization in future nanoelectronics.

3.2. Dimensional Crossover From Monolayer to Bulk

3.2.1. Stacking Types and Thickness-Dependence of 1T-PtSe$_2$

Stacking order of the sublayers in a layered material directly determines its structural, vibrational, electronic and optical properties. Therefore, theoretical prediction, prior to experimental synthesis, of stacking order is of importance.

Possible stacking orders in 1T-PtSe$_2$ crystal namely AA,(Pt atoms aligned on Pt atoms) AB,(Pt atoms aligned on Se atoms) A'A,(similar to AA but the top layer is upside-down) and A'B (similar to AB but the top layer is upside-down) are presented in Fig.3.3. It is found that energetically favorable stacking order is top to top (AA), as shown in Fig.3.3 (a). In addition, AB, A'A, and A'B, stackings are found to be 159, 321 and 91 meV, respectively, less favorable than the ground state structure. The lattice constant of AA stacked structure, 3.73 Å, is consistent with the experimentally reported value.(Wang *et al.*, 2015) Furthermore, the interlayer distances are calculated to be 2.14, 2.89, 3.61, and 2.63 Å for AA, AB, A'A, and A'B stacking orders, respectively.

It is also seen that while the thickness of single layer PtSe$_2$ is 2.68 Å, with additional layers thickness of each single layer is reduced and finally reaches to bulk value of 2.56 Å. Moreover, going from bilayer to bulk, the interlayer distance (vertical vacuum
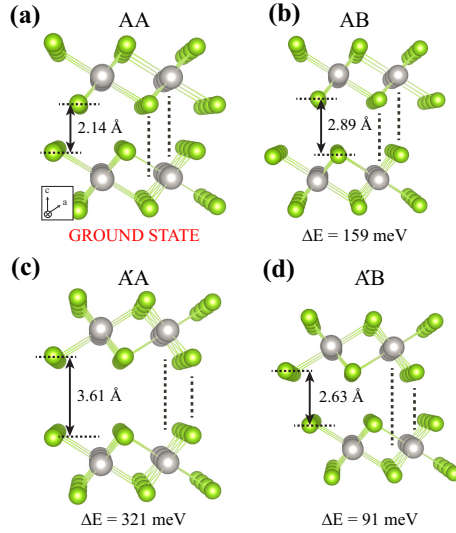
Figure 3.3. Top and side views of crystal structure of bilayer 1*T*-PtSe$_2$; AA, AB, A'A and A'B stacking orders.

spacing between the adjacent layers) also decreases from 2.14 to 2.07 Å. Apparently, there is an increasing trend in layer-layer interaction in the out-of-plane direction and therefore, as a result of thickness-driven compression, covalent Pt-Se bonds are enlarged. As listed in Table I, lattice constant of the bilayer, trilayer, four-layer, and bulk structures are found to be 3.73, 3.74, 3.75, and 3.77 Å, respectively. As monolayer PtSe$_2$, the ground state structure of the bilayer, trilayer, four-layer, and bulk structures is also found to be nonmagnetic. Therefore, thickness-dependence magnetization is absent in the PtSe$_2$ structures.

3.2.2. Thickness Dependence of Electronic Properties

In order to determine how the electronic characteristics are modified with increasing number of layers, we also calculate the electronic band dispersions of monolayer, bilayer, trilayer, and bulk PtSe$_2$. As shown in Fig. 3.4, going from monolayer to bilayer structure, the electronic band gap of the material rapidly decreases from 1.17 eV to 0.19 eV and it is also found that PtSe$_2$ crystals having thickness larger than the two layers all exhibit metallic behavior. In monolayer and bilayer structures of PtSe$_2$ the CBM states are composed of d state electrons that occupy d_{xy},d_{yz},d_{xz} and $d_{x^2-y^2}$ orbitals of Pt atom.

While the location of CBM in BZ remains same (at the Γ-M) when going from monolayer to bilayer, VBM is shifted from the Γ to the K-Γ high symmetry point. It is
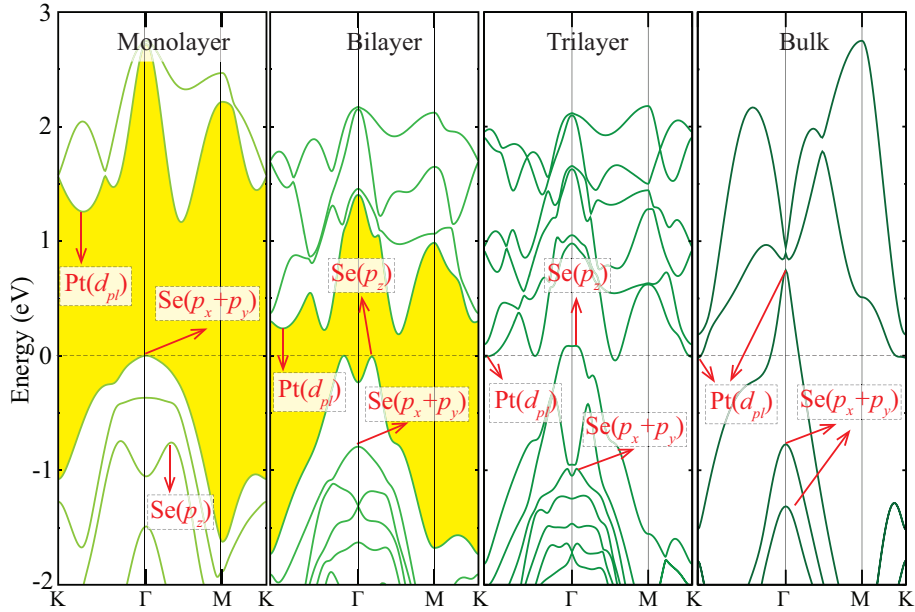
Figure 3.4. The electronic band dispersions of monolayer, bilayer, trilayer, bulk 1T-PtSe$_2$. The Fermi level is set to zero.

also worth to note that local minimum energy state of the CBM of the monolayer within the K-Γ translocates its position in the Brillouin Zone to the K symmetry point with the effect of additional layers. Rapid decrease in band energy of CB states and increase in VB states leads to metallization starting from trilayer.

On the other hand, the VBM state of the monolayer, that originates from p_x and p_y states of Se atoms, changes its energy space and takes position at the states energetically lower than the VBM state of the few-layer PtSe$_2$. Moreover, the VBM state of the bilayer, which consists of p_z orbitals of Se atoms, crosses Fermi level and becomes one of the metallic transition band at the few-layer PtSe$_2$, as seen in the first case same trend appears in the p_z orbitals of the Se atoms. It is obviously seen that the nesting in the corresponding state disappears while number of layer of PtSe$_2$ increases.

In addition, the work function values of bilayer, trilayer, four-layer, and bulk structures are found to be 4.64, 4.67, 4.72, and 4.76 eV, respectively. The reason of a sudden decrease from monolayer to bilayer in the work function value is related to rising of p_z orbitals of Se atoms from monolayer to bilayer. Then, increasing work function trend from bilayer to bulk is an expected behavior due to decrease in surface to bulk ratio of the structure.

3.2.3. Thickness Dependence of Vibrational Properties

Investigation of the vibrational properties not only allows one to deduce the dynamical stability of the structure but also allows determination of characteristic properties such as bond strengths, layer thickness and polarizability. In this subsection, thickness dependency of phonon band dispersions, Raman intensities and eigen-frequency shifts of the prominent peaks of bilayer, trilayer, four-layer and bulk $PtSe_2$ are investigated.

Figs. 3.5 (a)-(d) show the calculated phonon band structure of bilayer, trilayer, four-layer and bulk $PtSe_2$. It is seen that all the phonon modes have real eigenfrequencies, which indicate that bulk and few-layered $PtSe_2$ are stable. The appearance of small imaginary frequencies (less than 5 cm^{-1}) near the gamma point are not an indication of instability, they are numerical artifacts caused by the inaccuracy of the FFT grid. As shown in Fig. 3.5 (a)-(d), while LA modes cross the low-frequency optical modes, highest-frequency dispersionless optical modes are well-separated from low-lying phonon branches. Computationally predicted modes at 152.2 and 212.5 cm^{-1} correspond to the E_g and A_{1g} phonons of bulk $PtSe_2$ are in good agreement with previous experimental results indicating the reliability of computational methodology of phonons. As shown in the Fig. 3.5, in addition to the E_g and A_{1g} modes of the monolayer structure, additional peaks with low frequencies correspond to shear (S) and layer-breathing (LB) appear with the increasing thickness. It is found that S and LB modes are Raman active and as the number of layer increases from bilayer to bulk, the frequencies of S and LB modes increase from 38.8 and 44.0 cm^{-1} to 55.0 and 74.3 cm^{-1}, respectively.

It is also worth noting that, as shown in Fig. 3.5 (e), Raman vibrational characteristics of the E_g phonon strongly depend on the material thickness. It appears that, with increasing thickness, layer-layer interaction originated compression on each sublayer yields two consequences in $PtSe_2$; (i) phonon softening due to enlarged Pt-Se bonds and (ii) increasing Raman activity due to enhanced polarizability.

It is also seen from Fig. 3.5 (f), when the number of layers is increased, A_{1g} peak hardens while E_g peak softens. The downshift in the frequency of E_g peak is ascribed to the change in the dielectric screening environment for long-range Coulomb interactions as the thickness of the material increases. However, the upshift in the frequency of A_{1g} peak is attributed to increasing interlayer interactions which enhance the restoring forces on the atoms.(Lee *et al.*, 2010; Molina-Sanchez and Wirtz, 2011) Therefore, the strong layer dependency of Raman intensity of E_g mode and peak positions of E_g and A_{1g} modes can be used to determine the material thickness.
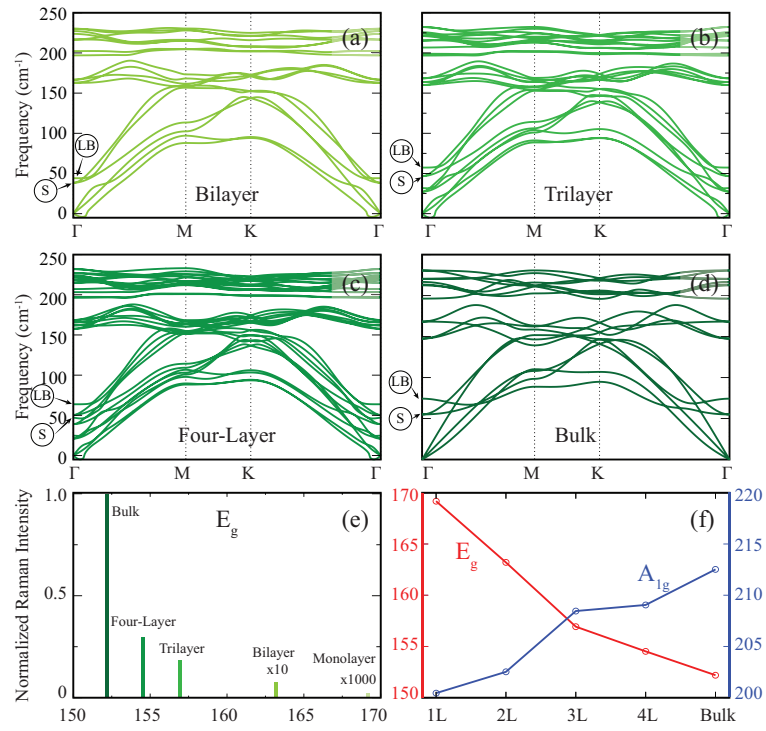
Figure 3.5. The phonon band dispersions of bilayer, trilayer, four-layer and bulk.

CHAPTER 4

SINGLE-LAYER JANUS PLATINUM DICHALCOGENIDES

4.1. Single-Layers of PtX2

4.1.1. Structural Properties

The atomic structures of PtX_2 are shown in Fig. 4.1(a). The single-layer PtX_2 crystal structures exhibits hexagonal symmetry and trigonal primitive unitcell in their 1T phase in which each Pt atom is surrounded by six X atoms forming a near-octahedral $[PtX_6]^{4-}$ unit. For single-layer PtS_2, $PtSe_2$, and $PtTe_2$, the optimized lattice parameters ($a=b$) are calculated to be 3.57, 3.69 and 3.92 Å, respectively. As presented in Table 5.2, the length parameters in the structural properties such as bond distances and geometric thickness (which is defined to be the vertical distance between uppermost and lowermost chalcogenide atoms) enlarge with the increasing atomic radius. The cohesive energy per formula in the unitcell is calculated to be 4.68 eV for single-layer PtS_2, whereas those for $PtSe_2$ and $PtTe_2$ are found as 4.42 and 4.28 eV, respectively. As the atomic radius of the chalcogenide atom increases from S to Te, the bond length between Pt-X atoms increases which reveals the existence of relatively weaker bonds that means the required energy to remove the chalcogenide atom from the structure decreases.

According to Bader charge analyses, formation of single-layer PtS_2 can occur by donation of 0.4 e^- from each Pt atom to S atoms. In addition, while $PtTe_2$ single-layer is formed by 0.3 e^- transfer from each Te to Pt atom, in $PtSe_2$ crystal structure bonds are formed without any charge transfer between Pt and Se. Apparently, $PtSe_2$ single-layer has entirely covalent bonds while PtS_2 and $PtTe_2$ have partially ionic bonding character.

4.1.2. Raman Activity, Elastic and Electronic Properties

The dynamical stability of the single-layer $1T-PtX_2$ structures are verified by calculating their phonon band structures through the whole BZ. As shown in Fig. 4.1(b),
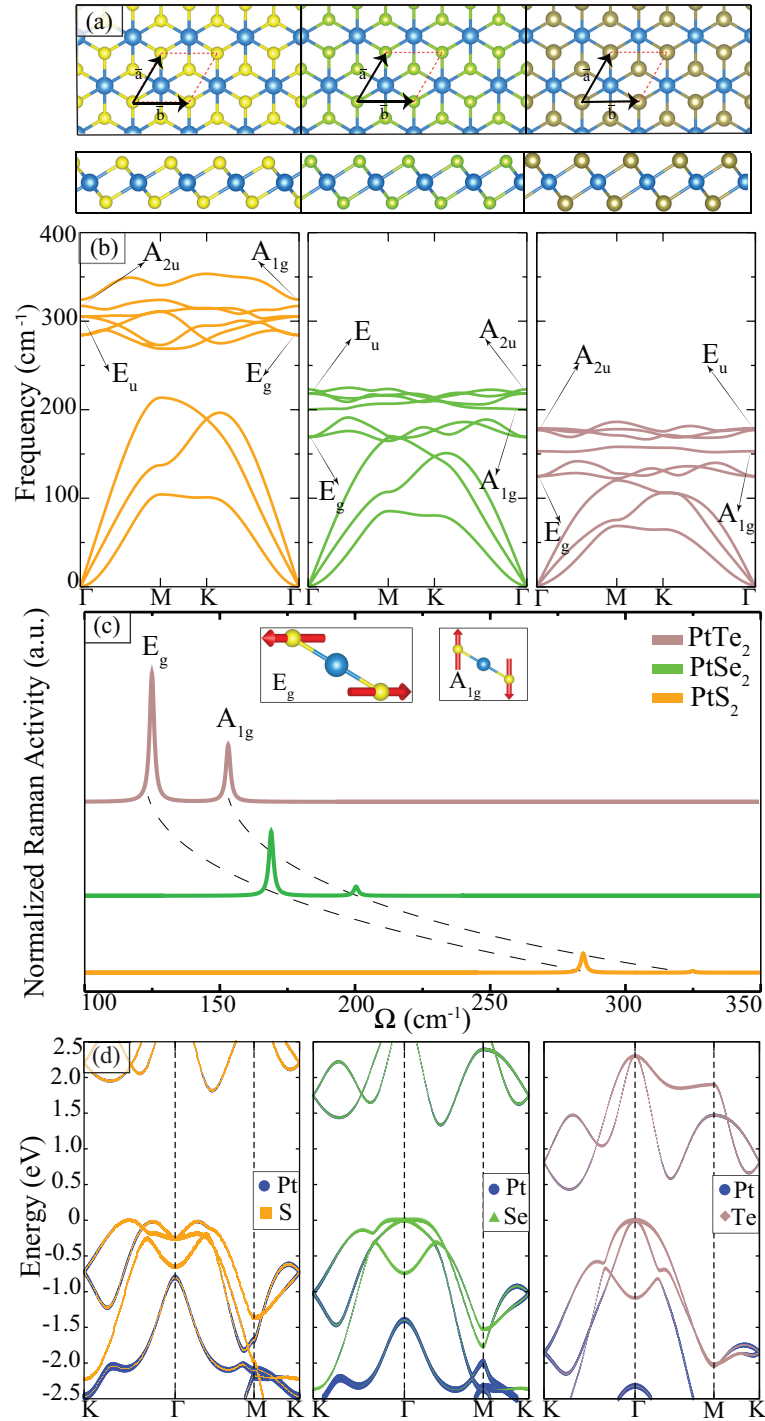
Figure 4.1. Geometric structures, phonon and electronic band diagrams of PtS$_2$, PtSe$_2$, and PtTe$_2$. Yellow, blue, green, and brown colors show S, Pt, Se, and Te atoms, respectively.

Table 4.1. The calculated parameters for single-layers of PtS$_2$, PtSe$_2$, and PtTe$_2$ are: the lattice constants, $a=b$; the atomic distance between Pt and X atoms (X=S, Se, Te), d; the thickness of single-layer, h; the cohesive energy per atom, E$_{Coh}$; the charge donation from Pt to chalcogenide atom, $\Delta\rho$; work function, Φ; total magnetic moment, μ.

	$a=b$ (Å)	d (Å)	h (Å)	E$_{Coh}$ (eV)	$\Delta\rho$ (e^-)	Φ (eV)	μ (μ_B)
PtS$_2$	3.57	2.40	2.46	4.68	0.4	6.07	0
PtSe$_2$	3.69	2.52	2.68	4.42	0.0	5.36	0
PtTe$_2$	3.92	2.69	2.90	4.28	-0.3	4.30	0

all single-layers of PtX$_2$s are free from imaginary frequencies in the whole BZ, indicating that they are dynamically stable. In the 3-atom primitive unitcell, each single-layer exhibits nine phonon branches three of which are acoustic and the remaining six have optical character.

While there is a large gap ($\sim$55 cm^{-1}) between acoustic and optical phonon branches of PtS$_2$, for PtSe$_2$ and PtTe$_2$ crystals mid-frequency optical modes overlap with acoustic modes at the M symmetry point. As a result of the planar symmetry in 1T phase, six optical modes in PtX$_2$ structures consist of two doubly degenerate in-plane and two non-degenerate out-of-plane phonon modes. For the single-layer PtS$_2$, the out-of-plane modes A$_{2u}$ and A$_{1g}$ occur at frequencies 317.3 cm^{-1} and 324.4 cm^{-1}, respectively while two doubly degenerate in-plane modes: E$_g$ and E$_u$ have frequencies 284.3 cm^{-1} and 305.2 cm^{-1}, respectively at the Γ point. In addition, single-layers of PtSe$_2$ and PtTe$_2$ have A$_{2u}$ (223.0 and 177.0 cm^{-1}, respectively), A$_{1g}$ (200.5 and 153.1 cm^{-1}, respectively) out-of-plane phonon modes, while they have two doubly degenerate E$_g$ (169.1 and 124.8 cm^{-1}, respectively) and E$_u$ (218.3 and 178.8 cm^{-1}, respectively) in-plane modes.

The group theory analysis reveal that 1T-PtX$_2$ which belongs to the D$_{3d}$ point group possess three Raman active phonon modes. The optical phonon modes, E$_g$, are attributed to the in-plane vibration of chalcogenide atoms against each other while the non-degenerate A$_{1g}$ mode represents the out-of-plane vibration of chalcogenide atoms against each other (see the inset of Fig. 4.1(c). For the two optical phonon modes, A$_{1g}$ and E$_g$, the force constant per unit area can be related to the phonon frequency by the equations(Zhang *et al.*, 2013);

$$\Omega_{A_{1g}} = \left(\frac{1}{2\pi c} \right) \sqrt{\frac{2\alpha_{Pt-X}^{\perp}}{\mu}},$$

$$\Omega_{E_g} = \left(\frac{1}{2\pi c} \right) \sqrt{\frac{2\alpha_{Pt-X}^{\parallel}}{\mu}}, \tag{4.1}$$

where μ is the atomic mass per unit area and c is the speed of light. Due to the contribution of only chalcogenide atoms to the vibration, the total mass per unit area is equal to $2m_X$.

The calculated mass per unit area is 0.5×10^{-6}, 1.1×10^{-6}, and 1.6×10^{-6} (kg/m^2) for PtS$_2$, PtSe$_2$, and PtTe$_2$, respectively. As seen from Table 4.2, when going from PtS$_2$ to PtTe$_2$, the heavier the chalcogen atom the smaller the force constants which is directly attributed to the weaker bonds formed by heavier chalcogenide atom. Therefore, soft crystals formed by heavier chalcogenide atoms display remarkable phonon softening in their spectrum as shown in Fig. 4.1(b).

In all single-layers, the Raman activity of A$_{1g}$ mode is smaller than that of E$_g$ modes which occurs due to the relatively smaller contribution of ϵ_{zz} to the Raman tensors(Yagmurcukardes *et al.*, 2018). In order to make a comparison between different single-layers, the Raman activities are normalized to the volume of each primitive unit-cell. As seen in Fig. 4.1(c), the Raman activity of each mode increases from PtS$_2$ to PtTe$_2$. Relatively larger atomic bond lengths result in larger dielectric constant which exhibits larger change of polarizability in the crystal when subjected to an incident light. Hence, increasing Raman activity of the phonon modes from PtS$_2$ to PtTe$_2$ can be attributed to the increase in macroscopic static dielectric constants (see Table 4.2).

4.1.3. Linear-Elastic Properties

The linear-elastic properties of 2D single-layer materials can be represented in terms of two independent constants; the in-plane stiffness, C, and the Poisson's ratio, ν. For determination of linear-elastic constants via energy-strain relation a 54-atom supercell is constructed for each crystal structures. Biaxial and uniaxial strains are applied for both tensile and compressive cases. The strain parameters ε_a and ε_b are varied between ± 0.015 with a step size of 0.005. Then, three different sets of data are calculated; (i) ε_a=0 and ε_b varying, (ii) ε_b=0 and ε_a varying and (iii) ε_a=ε_b varying. At each configuration, the atomic positions are fully relaxed and the strain energy, E_S, is calculated by subtracting

the total energy of the equilibrium state from the strained structure. Then, the calculated data is fitted to the equation; $E_S = c_1\varepsilon_a{}^2 + c_2\varepsilon_b{}^2 + c_3\varepsilon_a\varepsilon_b$(Nye$et$ $al.$, 1985), and the coefficients, c_i, are determined. Therefore, the in-plane stiffness, C, the measure of the rigidity of a material under applied external load, can be calculated by the formula; $C = (1/A_0)(2c - c_3{}^2/2c)$(Kang et $al.$, 2015) where c_1=c_2 due to the in-plane isotropy and A_0 is the area of the unstrained supercell. As listed in Table 4.2, the C values are 99, 88, and 73 N/m from single-layer PtS$_2$ to PtTe$_2$. In agreement with the calculated in-plane component of intra-layer force constants ($\alpha^{\parallel}_{Pt-X}$); the larger the bond lengths, the smaller the in-plane stiffness. This decreasing trend demonstrates that as the in-plane stiffness decreases, the corresponding restoring forces in the structure become effective in a shorter range of applied strain, i.e. the harmonic strain region gets smaller for soft materials. A similar trend for in-plane stiffness values were reported in CMR data base(Haastrup et $al.$, 2018) (86, 71, and 65 N/m from single-layer PtS$_2$ to PtTe$_2$). Here slightly different values obtained by different theoretical methodologies can be better explained via experimental measurements.

In addition one can obtain the Poisson's ratio defined as the ratio of the transverse contraction strain to the longitudinal extension strain in the direction of the stretching force. Here the Poisson's ratio for a- and b-vectors are calculated in terms of the coefficients c_i as; ν_a=ν_b=$c_3/2c$. The Poisson's ratios display small changes from single-layer PtS$_2$ to PtTe$_2$ (0.29 for PtS$_2$, 0.31 for PtSe$_2$, and 0.31 PtTe$_2$). When compared with well-known TMDs, i.e. 0.25 for MoS$_2$(Guzman and Strachan, 2014), 0.22 for WS$_2$(Guzman and Strachan, 2014), and 0.23 for MoSe$_2$(Guzman and Strachan, 2014), PtX$_2$ crystals exhibits larger responses to the applied load along the perpendicular direction. Such relatively large Poisson's ratios suggest more sensitive structural response to external loads which can be beneficial for nanoelastic applications.

4.1.4. Electronic Structure

The electronic band dispersions of the single-layers of 1T-PtX$_2$ through the whole BZ are shown in the Fig. 4.1(d). It is found that all structures are indirect band gap semiconductors. The indirect band gaps of PtS$_2$, PtSe$_2$ and PtTe$_2$ are calculated to be 1.82, 1.34 and 0.34 eV, respectively. Therefore, the band gaps are inversely proportional to the atomic mass of their chalcogenide types. The VBM of single-layer PtS$_2$ resides between the K and Γ points while that of the other single-layers are located at the Γ point. It is seen from the Fig. 4.1(d) that the VBM takes the shape of a sharper concave
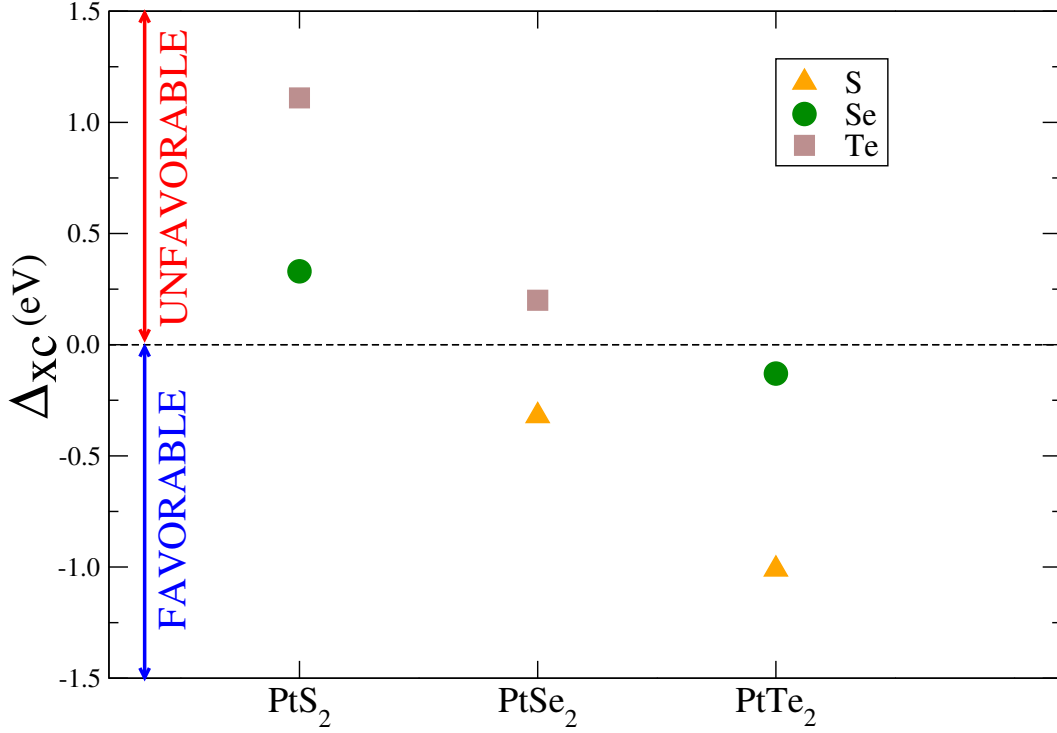
Figure 4.2. The exchange energy formed by the transverse process between a host and a foreign chalcogenide atom in a large-scale platinum dichalcogenide single-layer.

from PtS_2 to $PtTe_2$ with increasing effective mass. CBM shifts from within the Γ-M to within the Γ-K. The CBM of single-layer PtS_2 and $PtSe_2$ reside between the M-Γ points while the CBM of single-layer $PtTe_2$ reside between the Γ and K points. As seen from the Fig. 4.1(d) the CB edge in between the Γ and K points becomes energetically more favorable as the radius of the chalcogenide atom increases and it becomes CBM for single-layer $PtTe_2$. This behavior may be attributed to the increasing lattice parameters in the structure when compared to those of PtS_2 and $PtSe_2$.

4.1.5. Chalcogen Exchange in Single-layers PtX_2

The exchange energies required to replace a single chalcogenide atom instead of the host chalcogenide atom are shown in Fig. 4.2. The exchange energy is calculated by replacing a foreign chalcogenide atom to a host chalcogenide atom in a $3 \times 3 \times 1$ supercell by using the formula; $E_{exc} = E_{tot}(Pt_9X_{18}) - E_{tot}(Pt_9X_{17}X'_1) - E_{tot}(Xâ)$ where $E_{tot}(Pt_9X_{18})$ is the total energy of 3×3 supercell of the bare PtX_2 while $E_{tot}(Pt_9X_{17}X'_1)$ is that of the

Table 4.2. The calculated parameters for single-layers of PtS$_2$, PtSe$_2$, and PtTe$_2$ are: frequencies of Raman-active phonon modes A$_{1g}$ and E$_g$; intra-layer force constant per unit area between Pt and X atoms, out-of-plane ($\alpha^{\perp}_{Pt-X}$) and in-plane ($\alpha^{\parallel}_{Pt-X}$) components; in-plane and out-of-plane macroscopic static dielectric constants, ϵ_{xx}=ϵ_{yy} and ϵ_{zz}; in-plane stiffness, C; and Poisson's ratio, ν.

	A$_{1g}$ (cm^{-1})	E$_g$ (cm^{-1})	$\alpha^{\perp}_{Pt-X}$ (N/m^3)	$\alpha^{\parallel}_{Pt-X}$ (N/m^3)	ϵ_{xx}=ϵ_{yy} —	ϵ_{zz} —	C (N/m)	ν —
PtS$_2$	324.4	284.3	1.9×10^{21}	1.4×10^{21}	3.97	1.22	99	0.29
PtSe$_2$	200.5	169.1	1.6×10^{21}	1.1×10^{21}	7.52	1.50	88	0.31
PtTe$_2$	153.1	124.8	1.3×10^{21}	0.9×10^{21}	10.64	1.61	73	0.31

exchanged structure and E$_{tot}$(Xâ) is the total energy of replaced chalcogenide atom in vacuum. By examining such exchange energy, it is possible to determine whether the replacement is obtained with or without external energy.

As seen in Fig. 4.2, when one S atom is replaced by Se or Te in a single-layer PtS$_2$, the exchange energies are found to be 0.33 and 1.11 eV, respectively. On the other hand, if S or Te exchanges with a Se atom in the PtSe$_2$, the required energies are calculated to be -0.32 and 0.20 eV, respectively. The minus sign indicates the process is exothermic, whereas the positive sign means that an additional energy is required and the process is endothermic. In single-layer PtTe$_2$, the exchange of chalcogenide atoms, with S or Se atoms is found to require -0.13 and -1.03 eV, respectively. It is clearly seen that the exchanging a small chalcogenide atom instead of a larger chalcogenide atom is energetically favorable process. It is found that the replacing S atoms instead of Te atoms in single-layers of PtTe$_2$ is the energetically most favorable process.

4.2. Janus type Single-layers of XPtY

4.2.1. Structural Properties

Janus type ultra-thin platinum dichalcogenides are constituted completely two different chalcogenide surfaces. After a detailed analysis of single-layer 1T-PtX$_2$, we investigate the 1T phase of Janus, or in other words, ternary platinum dichalcogenide single-layer structures, 1T-XPtY. Fig. 4.3 shows the crystal structure of the single-layer 1T-XPtY.

In a Janus structure, platinum is sandwiched between upper chalcogenide (X) and bottom chalcogenide (Y) layers in 1T-phase.

As given in Table 4.3, the calculated lattice parameters ($a=b$) of ternary platinum dichalcogenides are 3.63, 3.75 and 3.81 Å for SePtS, TePtS and TePtSe, respectively. The atomic bond lengths between Pt atom and the upper (Se) and lower sides (S) are 2.50 and 2.43 Å in SePtS structure. On the other hand, for TePtS structure, the Pt-Te bond length is 2.62 Å while that of Pt-S is 2.57 Å. In single-layer TePtSe, the atomic bond lengths Pt-Te and Pt-Se are calculated as 2.64 and 2.57 Å, respectively. Moreover, the thicknesses are found to be 2.57, 2.70 and 2.80 Å for SePtS, TePtS, and TePtSe, respectively. In addition, the calculated cohesive energies are 4.53, 4.40 and 4.31 eV, for SePtS, TePtS and TePtSe, respectively. As we discussed in Section 3A, the same trend between cohesive energies and bond lengths in the structure are found for the Janus single-layers which is a result of the existing chalcogenide atoms in the Janus crystal.

It is seen that when a small atom is placed inside the structure instead of a large atom, lattice parameters, the bond lengths, the thickness, and the cohesive energies decrease accordingly. According to Bader charge analyses, in single-layer SePtS Pt donates 0.2 e^-, S receives 0.2 e^-, and Se has no charge transfer. Since charge transfers are obtained for TePtS and TePtSe, it is seen that Te donates 0.1 e^- to Pt and 0.3 e^- to S in TePtS, in TePtSe while Te donates 0.2 e^- to Pt and 0.1 e^- to Se.

4.2.2. Janus Structures via Phonons and Raman Spectra

To verify dynamical stability of the Janus platinum dichalcogenide structures, the vibrational properties of the XPtY single-layers are investigated and the phonon band diagrams are shown in Fig. 4.3(b). Similar to their binary analogs, Janus structures are also found free from the imaginary frequencies in the whole BZ indicating their dynamical stability. In addition, Janus single-layers exhibit three acoustical and six optical phonon branches.

As shown in Fig. 4.3(b), the phonon band gaps are $\sim$ 27, 36 and 14 cm^{-1} for single-layer SePtS, TePtS, and TePtSe, respectively. The phonon band gaps of XPtY structures become narrower and the phonon bands soften from SePtS to TePtS and TePtSe. This can also be attributed to different atomic masses, as the mass of chalcogenide atom increases the corresponding vibrational frequencies decrease.

Differing from the single-layers of PtX$_2$ crystals, single-layers of XPtY Janus structures exhibit additional Raman active phonon modes originating from the broken in-
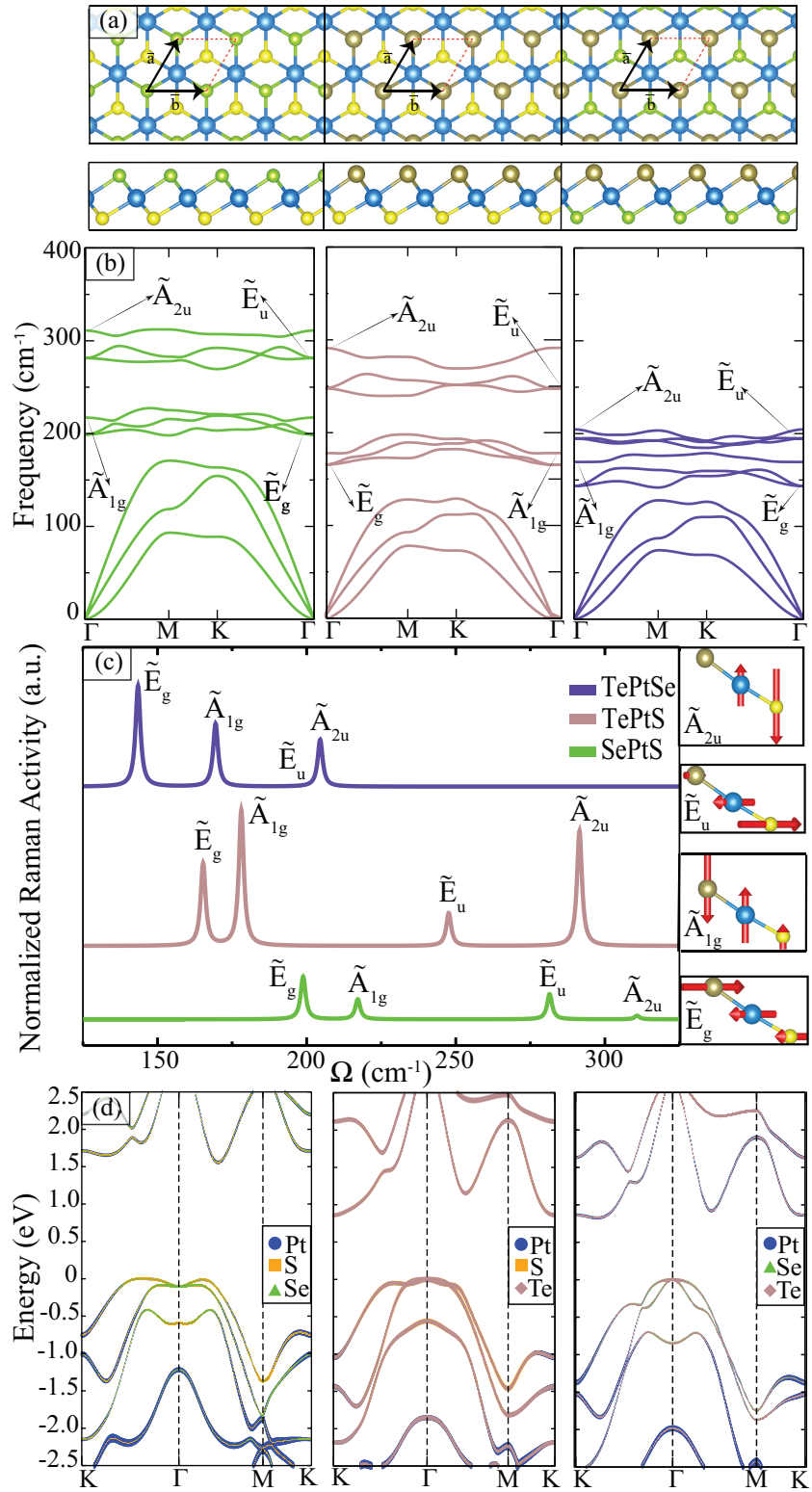
Figure 4.3. The geometric structures, phonon diagrams and electronic band structures of SePtS, TePtS, and TePtSe

version symmetry. The single-layers of XPtY structures exhibit six Raman active phonon modes two of which are non-degenerate out-of-plane modes while the remaining four are doubly-degenerate having in-plane vibrational character. Since the two chalcogenide atoms are different, their vibrations with respect to the Pt layer are not symmetric. Thus, depending on the atomic mass, i.e. on the atomic bond lengths, the Raman activities differ from one structure to another. For instance, the phonon mode $\widetilde{A}_{2u}$ has the smallest Raman activity when the total Pt-X bond length is the smallest, i.e. for single-layer SePtS structure. The activity of this mode gets larger for single-layer SPtTe and decreases for single-layer SePtTe. The reason for this behavior is the vibrational character of the atoms in the phonon mode. As seen on the right panel of Fig. 4.3(c), one of the chalcogenide atoms is stationary and do not contribute to the vibration. In S-based XPtY structures, Raman activity increases from SePtS to TePtS because of the increasing mass of stationary chalcogenide atom. By the same analogy, the $\widetilde{E}_u$ mode exhibits the same behavior since it represents the in-plane vibration of Pt and lighter chalcogenide atoms. For the $\widetilde{A}_{1g}$ mode the same trend is found because in S-based XPtY structures the vibration of Se and Te atoms dominate that of S atom. When the second chalcogenide atom is changed from Se to Te, the dipole between Pt and Te atoms increases due to the larger atomic bond in Pt-Te. Therefore, the Raman activity of the $\widetilde{A}_{1g}$ increases from SePtS to TePtS. However, in single-layer TePtSe the vibration of Pt and Se atoms have almost the same strength while the vibration of Te dominates the motion. Finally, when we analyze the $\widetilde{E}_g$ mode, it is seen that the Raman activity increases from SePtS to TePtSe. In all single-layer XPtY structures, the Pt atom and the lighter chalcogenide atom vibrate along the same direction while the heavier chalcogenide atom vibrates in opposite direction. Therefore, the Raman activity increases when the bond length between Pt and the heavier chalcogenide atom increases.

Table 4.3. The calculated parameters for single-layers of SePtS, TePtS, and TePtSe are: the lattice constants, $a=b$, the atomic distance between Pt and X atoms (X=S, Se, Te), d; the thickness of single-layer, h; the cohesive energy per formula, E_{Coh}; the charge donation from Pt to chalcogens, $\Delta\rho$.

	$a=b$ (Å)	d_{Pt-Se} (Å)	d_{Pt-S} (Å)	d_{Pt-Te} (Å)	h (Å)	E_{Coh} (eV)	$\Delta\rho$ (e^-)
SePtS	3.63	2.50	2.43	-	2.57	4.53	0.2
TePtS	3.75	-	2.57	2.62	2.70	4.40	-0.1
TePtSe	3.81	2.57	-	2.64	2.80	4.31	-0.2

4.2.3. Elastic and Electronic Properties

Using the same methodology, the in-plane stiffness and Poisson's ratio are calculated for the Janus type single-layer structures. As listed in Table 4.4, the C values are 93, 78, and 76 N/m for SePtS, TePtS and TePtSe, respectively. Apparently, the larger the interatomic distance, the smaller the stiffness. The decreasing trend of the in-plane stiffness also matches well with the change in cohesive energy. When these values are analyzed in terms of the individual in-plane stiffness and Poisson's ratio, in all single-layers XPtYs the in-plane stiffness is determined by heavier chalcogenide atom. It is seen that the Te-based single-layers of XPtY, TePtS and TePtSe, exhibit the same ν (0.31) values which are dominated by the Te atom while for the single-layer of SePtS the ν is found to be close to that of PtS_2.

The electronic band diagrams of single-layer XPtY are shown in Fig. 4.3(d). It is seen that Janus structures of SePtS, TePtS and TePtSe are indirect band gap semiconductors with band gap of 1.56, 0.86 and 0.82 eV, respectively. In Janus structures replacement of small atoms by larger atoms simply leads to the narrowing of the band gap. While the band structure of SePtS is detemined by both and S and Se states, electronic bands of Te-including Janus single-layers mainly composed of Te states. Compared with their binary analogs, character of VBM and CBM in single-layer XPtY structures are significantly different. It is seen that VBM of Janus structures shifts to the Γ point and take the shape of a sharper concave from SePtS to TePtSe with increasing effective mass. However, differing from the binary analogs, CBM of Janus structures shifts from the Γ-M to the K symmetry point.

Table 4.4. The calculated parameters for single-layers of SePtS, TePtS, and TePtSe are: work function, Φ; net magnetization in the primitive cell, μ; in-plane and out-of-plane macroscopic static dielectric constants, $\epsilon_{xx}=\epsilon_{yy}$ and ϵ_{zz}; in-plane stiffness, C; and Poisson's ratio, ν.

	Φ_{Pt-Se} (eV)	Φ_{Pt-S} (eV)	Φ_{Pt-Te} (eV)	μ (μ_B)	$\epsilon_{xx}=\epsilon_{yy}$ —	ϵ_{zz} —	C (N/m)	ν —
SePtS	5.31	6.09	-	0	6.80	1.46	93	0.30
TePtS	-	5.95	4.48	0	8.59	1.51	78	0.29
TePtSe	5.11	-	3.05	0	9.07	1.55	76	0.31
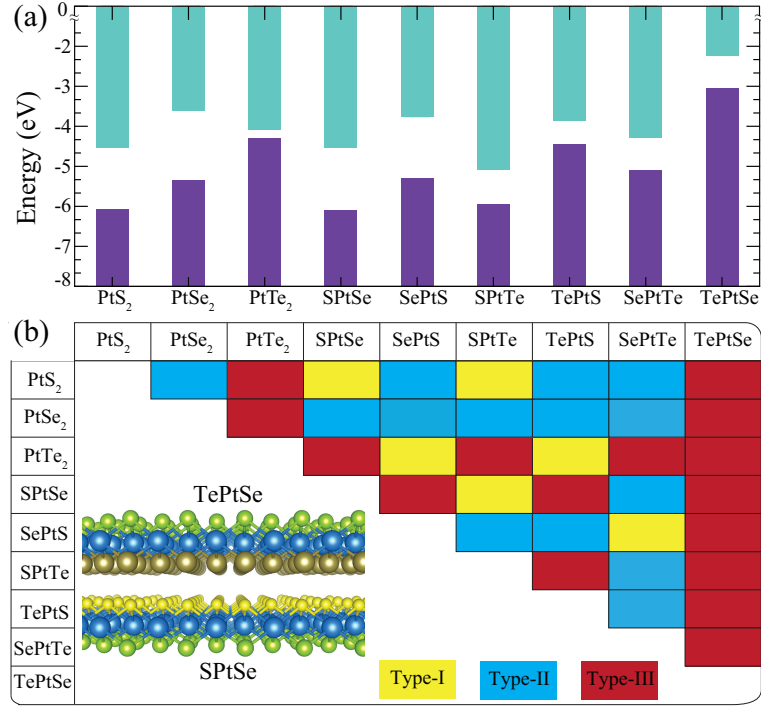
Figure 4.4. The band alignments of binary and ternary platinum dichalcogenides

4.2.4. Vertical van der Waals Heterostructures

Vertical vdW heterostructures of ultra-thin materials have been the focus of interest due to the idea of Lego type construction and combining properties of different single-layers in one structure.(Geim and Grigorieva, 2013; Novoselov *et al.*, 2016) Since binary and ternary platinum dichalcogenides are ultra-thin semiconductor materials, their vdW heterostructures and band alignments present broad variety to achieve different electronic characters. In this section, we focused possible vdW heterostructures and their electronic heterostructure types. Band alignments of binary and ternary (Janus type) platinum dichalcogenides are shown in Fig. 4.4.

In type-I (straddling) heterojunctions, VBM and CBM are from the same individual layer. These type heterostructures are common in superlattices and desirable for light emitting applications. As seen in Fig. 4.4(b), it is found that the type-I vdW heterostructures can be formed by PtS$_2$/SPtSe, PtS$_2$/SPtTe, PtTe$_2$/SePtS, PtTe$_2$/TePtS, SePtS/SePtTe and SPtSe/SPtTe.

If both VBM and CBM of one structure are lower than the VBM and CBM of the other structure, electrons are confined in one structure, while holes are confined in

the other structure. In this case, heterostructure type is called as type-II or staggered type heterojunction. Owing to separation of electrons and holes to different layers, the lifetime of radiative recombinations are increased; thus, these type heterostructures can be used for photocatalytic, photovoltaics and photodetection applications. PtS_2/$PtSe_2$, PtS_2/SePtS, PtS_2/SePtTe, PtS_2/TePtS, $PtSe_2$/SePtS, $PtSe_2$/SePtTe, $PtSe_2$/SPtSe, $PtSe_2$/SPtTe, $PtSe_2$/TePtS, SePtS/SPtTe, SePtS/TePtS, SePtTe/TePtS, SPtSe/SePtTe and SPtTe/SePtTe vdW heterostructures are found to form type-II heterojunctions.

In a type-III (broken) heterojunction, the CBM of one structure lies below the VBM of the other one. Such heterojunctions not only allow semimetal-to-semiconductor transitions but also lead to formation of interface excitons and coexistence electron and holes. We found that PtS_2/$PtTe_2$, PtS_2/TePtSe, $PtSe_2$/$PtTe_2$, $PtSe_2$/TePtSe, $PtTe_2$/SePtTe, $PtTe_2$/SPtSe, $PtTe_2$/SPtTe, $PtTe_2$/TePtSe, SePtS/TePtSe, SPtSe/TePtS, SPtSe/SePtS, SPtSe/TePtSe, SPtTe/TePtS, SPtTe/TePtSe, TePtS/TePtSe and TePtSe/SePtTe are type-III hetero-junctions.

CHAPTER 5

FUNCTIONALIZATION OF SINGLE LAYER TAS$_2$

5.1. Single-Layer of TaS$_2$

5.1.1. Structural Properties

The bulk forms of layered TaS$_2$ with phases trigonal 1T-TaS$_2$ (P$\bar{6}m$1), hexagonal 2H-TaS$_2$ (P$\bar{6}m$3), and rhombohedral 3R-TaS$_2$ (R$\bar{3}m$) have been widely investigated as the most common bulk phases. The optimized crystal structure of single-layer hexagonal 1H-TaS$_2$ is shown in Fig. 5.1(a). TaS$_2$ has a hexagonal crystal structure consisting of Ta layer sandwiched between two S layers. The optimized in-plane lattice parameters ($a = b$) are found to be 3.36 Å and is compatible with the previously reported atomic-resolution TEM observations.(Shi *et al.*, 2017). The bond length between Ta and S atoms is found to be 2.48 Å. Moreover, the thickness of TaS$_2$ monolayer (3.11 Å) is also close to the reported value of 2.92, described as distance between the upper and lower sides S.(Hinsche and Thygesen, 2017) As seen in table 5.1, cohessive energy of TaS$_2$ is found to be 6.27 eV/atom. Bader charge analyses show that each S atom receives 0.8 e^- from Ta atom.

5.1.2. Vibrational Properties

The calculated phonon band structure of single-layer TaS$_2$ is in agreement with the previous results (Hinsche and Thygesen, 2017). As shown in Fig. 5.1 (b), the phonon band dispersions are free from any imaginary frequencies through the whole BZ indicating the dynamical stability of TaS$_2$.(Thompson *et al.*, 1972) The three acoustic phonon branches are attributed as the out-of plane mode (ZA), the in-plane transverse mode (TA), and the in-plane longitudinal (LA). The remaining optical phonon modes(ZO) are in-plane transverse optic mode (TA), and in-plane longitudinal optic mode (LO), and the sequence is relative to increasing energy. The optical lattice-vibrational modes at the Γ point can be calculated by using the formula $\Gamma_{optical} = A_{1g} + A_{2u} + 2E_g + 2E_u$
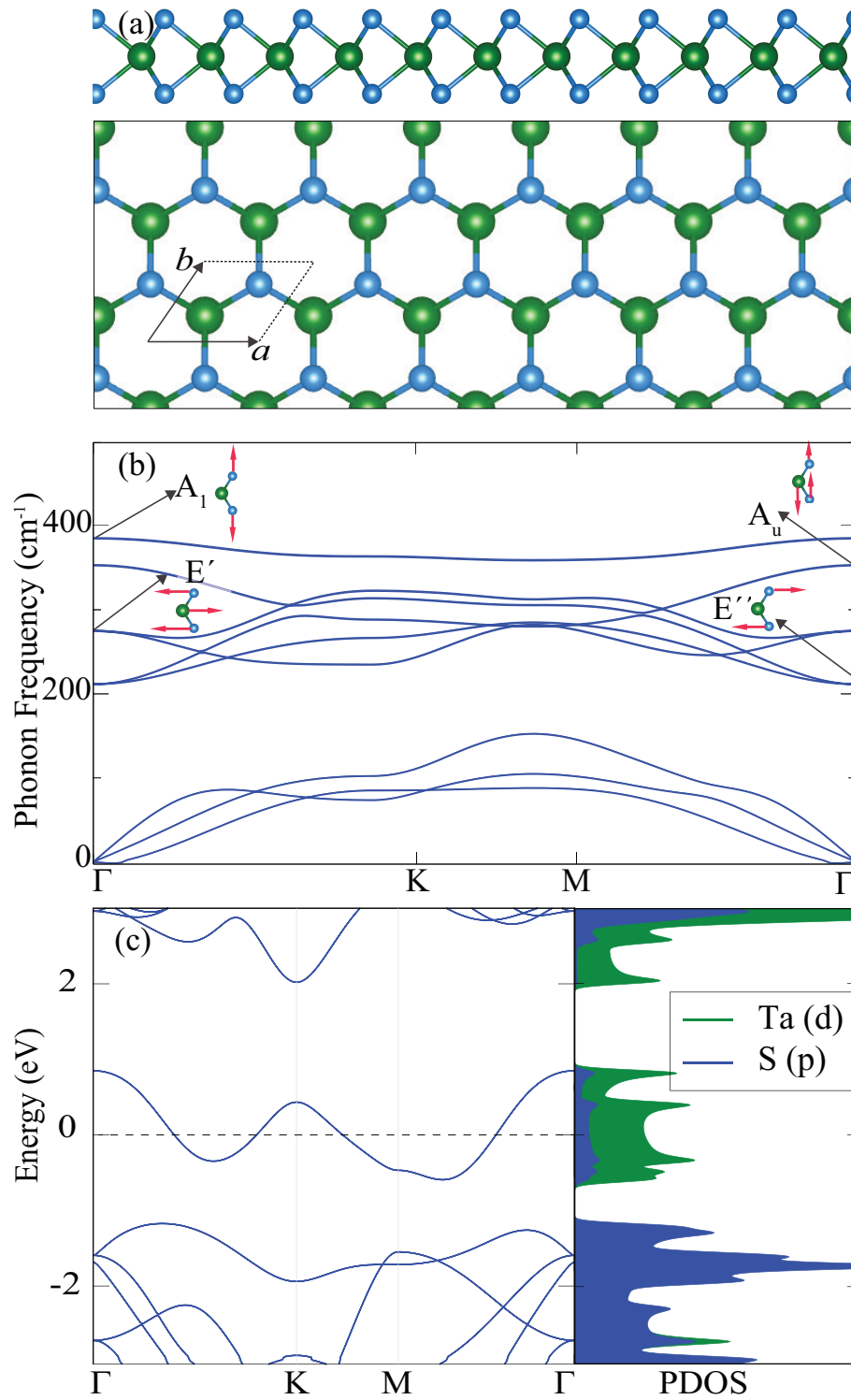
Figure 5.1. For single-layer TaS$_2$; the crystal, phonon and electronic band structure.

In terms of atomic mass, Ta is heavier compared to other TMDs and thus it lowers the vibration frequency while so a small gap outcomes in acoustic + acoustic + optic scattering much more frequently. Frequency gap between the optical and acoustic phonon branches in single-layer TaS$_2$ is 59 cm^{-1} . The optical phonon branches of single-layer TaS$_2$ consist of two doubly degenerate in-plane modes at 212 cm^{-1} (E_g) and 275 cm^{-1} (E_u), and two non-degenerate out-of-plane modes at 353 cm^{-1} (A_{2u}) and 385 cm^{-1} (A_{1g}) at the Γ point.

5.1.3. Electronic Properties

Fig. 5.1(c) shows the calculated electronic band structure and corresponding partial density of states (PDOS) of single-layer TaS$_2$. It is found that single-layer of TaS$_2$ has a metalic character with the nonzero density of states at the Fermi level and a high charge transfer between Ta $5d$ and S $4p$ (pd-hybridization). Previous experimental studies have demonstrated that TaS$_2$ is a metal.

Table 5.1. The calculated parameters for single-layers of TaS$_2$ structures, FTaS$_2$, HTaS$_2$, and Janus HTaS$_2$F are: the lattice constants, $a=b$; the atomic distance between S and X atoms (X=F, H), d; the thickness of single-layer, h; the cohesive energy per atom, E$_{Coh}$; initial and final charges of Ta, S, F, and H atoms, ρ_{Ta}, ρ_S, ρ_F, ρ_H; net magnetic moment per primitive cell, μ; and the energy band gap of the structures calculated, E$_{Gap}$.

	$a=b$	d_{Ta-S}	d_{S-F}	d_{S-H}	h	E$_{Coh}$
	(Å)	(Å)	(Å)	(Å)	(Å)	(eV/atom)
TaS$_2$	3.36	2.48	-	-	3.11	6.27
FTaS$_2$	3.43	2.41	1.65	-	4.55	5.38
HTaS$_2$	3.42	2.45	-	1.37	4.34	5.13
HTaS$_2$F	3.42	2.50	1.71	1.40	6.07	4.58
	ρ_{Ta}	ρ_S	ρ_F	ρ_H	μ	E$_{Gap}$
	(initial-final)	(initial-final)	(initial-final)	(initial-final)		
	(e^-)	(e^-)	(e^-)	(e^-)	(μ_B)	(eV)
TaS$_2$	5.0 - 3.4	6.0 - 6.8	-	-	0	-
FTaS$_2$	5.0 - 3.6	6.0 - 6.7	7.0 - 7.6	-	0	0.65
HTaS$_2$	5.0 - 3.6	6.0 - 6.7	-	1.0 - 1.0	0	0.96
HTaS$_2$F	5.0 - 3.6	6.0 - 6.4	7.0 - 7.6	1.0 - 1.0	0	-

5.2. One-Side Fluorinated TaS$_2$

The pioneering work of Nair *et al.*(Nair *et al.*, 2010) has shown that fluorinated graphene has been formed by laying fluorine successfully on graphene experimentally. The fluorinated graphene structure was reported to be teflon-like, semiconductor, and also flexible material. In another theoretical study, it has been shown that the form and composition of fluorine atoms play an important role in the alteration of properties such as binding energies, band spacings and phonon modes. Due to the electronic properties, the stable C$_2$F chair structure is metallic, while CF with non-magnetic character is insulator.(Şahin *et al.*, 2011)

5.2.1. Structural Properties

Fig. 5.2 (a) shows the atomic structure of single-layer FTaS$_2$, FTaS$_2$ belongs to P$\bar{6}m3$ space groups and has hexagonal Bravais lattice. As shown in table 5.1, the optimized crystal structure lattice parameter of the primitive unit cell FTaS$_2$ is 3.43Å, the thickness of single-layer FTaS$_2$ is 4.55Å, the corresponding Ta$-$S and S$-$F bond lengths are found to be 2.41Å and 1.65Å, respectively. Bader charge analysis shows that there is a charge transfer from Ta atom to S atom and F atom, Ta atom donates 0.7 and 0.6 e^- charges to S and F atoms, respectively. For single-layer of FTaS$_2$, the cohhesive energy is calculated to be 5.38 eV/atom.

5.2.2. Stability

To study the vibrational characteristics, phononic band dispersion of single-layer FTaS$_2$ is calculated. Structure of single-layer FTaS$_2$ is dynamical stable since all eigenfrequencies are real at whole BZ. FTaS$_2$ has four atoms in the unit cell. As seen in Fig. 5.2 (b), sigle-layer of FTaS$_2$ has twelve phonon branches, there of which are acoustic and the remaining nine of which are optical modes. There is a very small gap between the optic phonon modes and the acoustic phonon modes, 19 cm^{-1}. The formula defining the optical lattice vibration modes at the Γ point is as follows; $\Gamma_{optical} = \widetilde{E}_g + 2\widetilde{E}_u + 2\widetilde{A}_{2u} + \widetilde{A}_{1g}$.

Single-layer of FTaS$_2$ structure consists of three in-plane doubly degenerated and three out-of-plane phonon modes non-degenerated. Three degenerate in-plane modes; $\widetilde{E}_g$, $\widetilde{E}_u$, and $\widetilde{E}_u$ have frequencies 119 cm^{-1}, 262 cm^{-1}, and 355 cm^{-1}, respectively. However,

frequencies of three non-degenerate out-of-plane modes which are $\widetilde{A}_{2u}$, $\widetilde{A}_{2u}$, and $\widetilde{A}_{1g}$ are 290 cm^{-1}, 374 cm^{-1}, and 736 cm^{-1}, respectively.

5.2.3. Electronic Structure

As shown Fig. 5.2 (c), the electronic band dispersion and electronic density of states reveal that single-layer FTaS$_2$ starts to indicate semiconductor properties with 0.65 eV band gap with the effect of fluorination. It is found that FTaS$_2$ is an indirect band gap semiconductor. The valence band maximum (VBM) of single layer of FTaS$_2$ lies at K point while the conduction band minimum of single layer of FTaS$_2$ resides between the Γ and the K points. Excitonic transitions shifts due to indirect band gap from the K point. The electronic band and corresponding partial density of states calculations show that the conduction band states between the Γ and the K points are mainly due to localized p orbitals on both S and F atoms while the valance band states at the K point are mainly due to localized d orbitals on Ta atom.

5.3. One-Sided Hydrogenated TaS$_2$

It is an important method to use the chemical functionality to adjust the structural, electronic and magnetic properties of two-dimensional materials. It is common to use hydrogen atom for surface functionality. In a study by Elias *et al.*(Elias *et al.*, 2009), it was found that high conductivity graphene can be converted to an insulator by hydrogenating the surface of graphene. In another theoretical study it is shown that the band gap of TiSe$_2$ is opened and TiSe$_2$ exhibits a direct gap semiconductor behavior by the effect of hydrogenation. However, the effect of hydrogenation causes to a significant reduction in the heat capacity of the monolayer TiSe$_2$.(İyikanat *et al.*, 2017)

5.3.1. Structural Properties

The optimized atomic structure of single-layer of HTaS$_2$ is seen in Fig. 5.3 (a). Single-layer of HTaS$_2$ resembles a hexagonal structure of single-layer TaS$_2$ with Bravais lattice vectors, $\overrightarrow{a} = 0.5a(\sqrt{3}\widehat{x} - \widehat{y})$, $\overrightarrow{b} = 0.5a(\sqrt{3}\widehat{x} + \widehat{y})$, $\overrightarrow{c} = c\widehat{z}$. As shown in the table 5.1, lattice constants of the unit cell are calculated to be a=b= 3.42Å. The bond length between Ta atom and S atom is found to be 2.45Å, hydrogen is bonded to sulfide and the distance between them is 1.37 Å. Ground state of single-layer is formed with a cohessive energy of 5.13 eV/atom. Due to the Bader charge analysis, there is a total charge
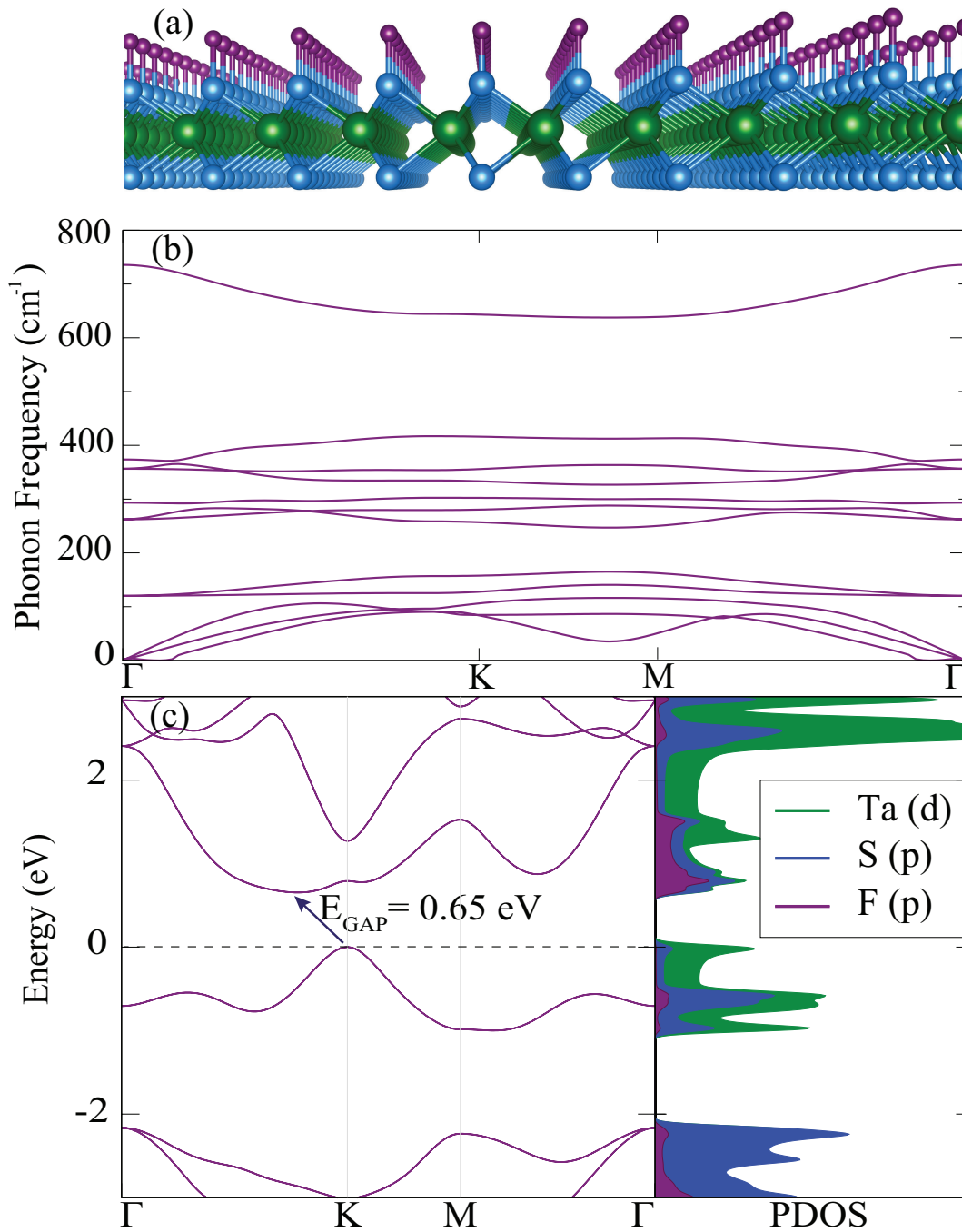
Figure 5.2. Perspective side view of one-sided fluorinated TaS_2. Phonon band diagrams of $FTaS_2$, Electronic band dispersion and PDOS of $FTaS_2$.

transfer of 1.4 e^- from Ta atom to S atom while there is no charge transfer between H atom and the other atoms.

5.3.2. Stability

Fig. 5.3 (b) shows that the structure is dynamically stable from the calculated eigenfunctions since all frequencies at whole BZ have real values. A three-dimensional crystal containing N atoms in the unit cell has 3N normal mode, 3N-3 of which are optical mode and the remaining 3 are acoustic modes. Since single-layer HTaS$_2$ four five atoms in the unit cell, HTaS$_2$ owns twelve phonon frequency branches, 3 of which are acoustic branches with low frequency and the remaining 12 are optical modes with higher frequency. There is a huge gap between acoustic and optic phonon branches, 126 cm^{-1}. The large phonon frequency gap is important for phonon scattering channel. Single-layer HTaS$_2$ include three degenerated in-plane modes optic phonon branches with 261 cm^{-1}, 321 cm^{-1}, and 470 cm^{-1} frequencies; $\widetilde{E}_g$, $\widetilde{E}_u$, and $\widetilde{E}_g$, respectively. Two of the non-degenerate out-of-plane optical are $\widetilde{A}_{2u}$ mode with frequencies 339 cm^{-1}, 378 cm^{-1} and the other is $\widetilde{E}_g$ mode with a frequency of 2440 cm^{-1}.

5.3.3. Electronic Structure

Fig. 5.3 (c) shows the electronic band dispersions and corresponding partial density of states of single-layer HTaS$_2$. Single-layer HTaS$_2$ is a semiconductor with an indirect band gap of 0.96 eV. It is found from the calculated PDOS that VBM states are mainly composed of the Ta-d orbitals and the S-p orbitals, while in the CBM states there is also the H-s orbital in addition to the S-p orbital of the Ta-d. In the electronic band diagram of the single-layer HTaS$_2$ is seen that the VBM is at point the M and the CBM is between the M and the Γ points.

5.4. Janus type Single-layer of TaS$_2$

5.4.1. Structural Properties

As shown in Fig. 5.4 (a), Janus type single-layer of TaS$_2$ is formed by two different surfaces with one face hydrogenated and the other face fluorinated. The janus type single-layer TaS$_2$ belongs to the space group P$\bar{6}m3$, similar to the other structures mentioned
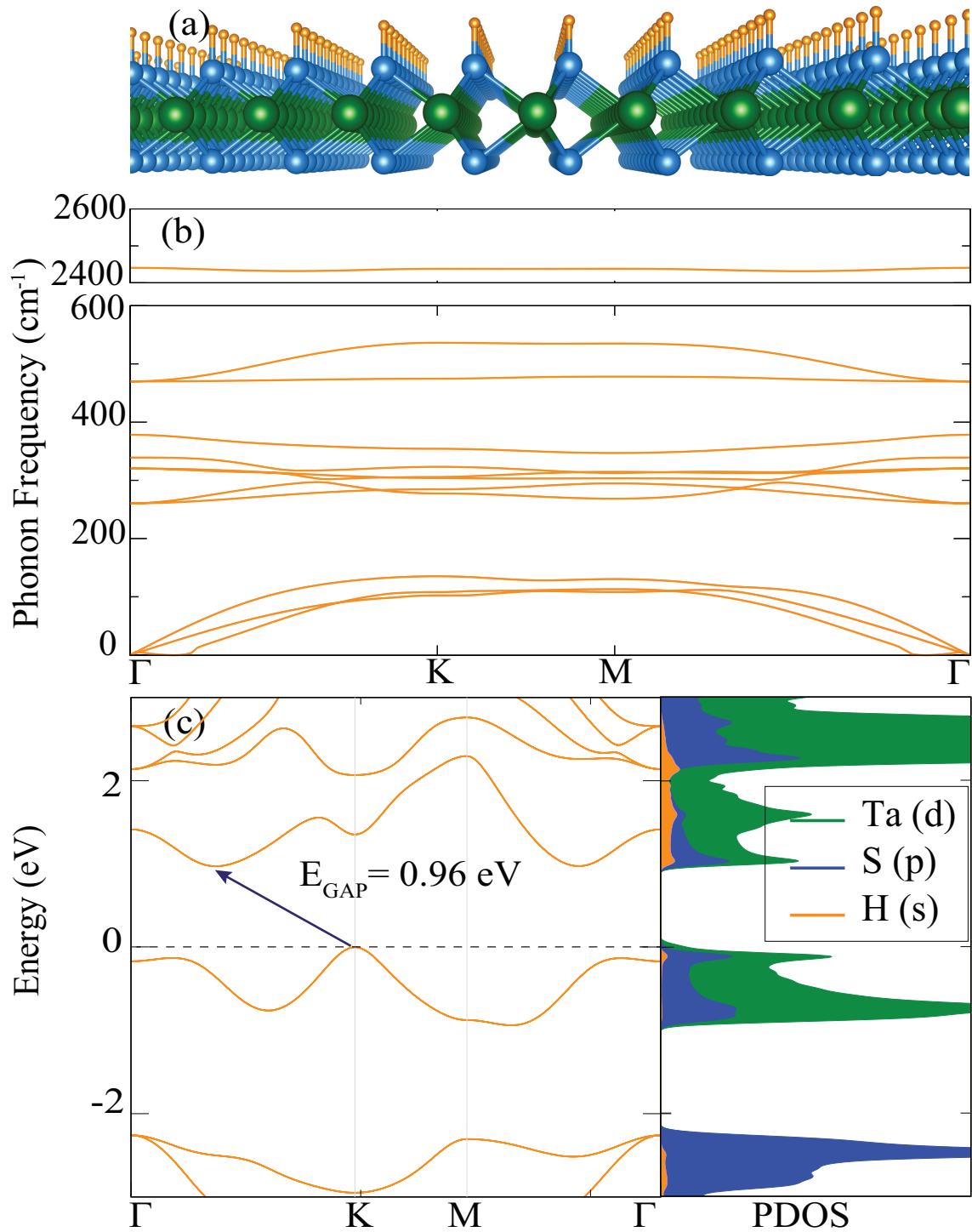
Figure 5.3. Perspective side view of one-sided hydrogenated TaS$_2$. Phonon band diagrams of HTaS$_2$, Electronic band structure and PDOS of HTaS$_2$.

above. Calculated structural parameters are as follows; optimized structure of $HTaS_2F$ is hexagonal structure with lattice parameter (a=b) 3.42 Å. The distance between the top and bottom layers is 6.07 Å. The length of the bond between the Ta atom and S atom is 2.50 Å and the lengths of the S atom with F and H atoms are 1.71 and 1.40 Å, respectively. Cohesive energy per atom is 4.58 eV for single-layer of Janus TaS_2. According to the Bader charge analysis, Ta atom donates 1.4 e^-, each S atom receive an average of 0.4 e^-, F atom received 0.6 e^-, and no charge transfer of H, as seen in Fig. 5.5 (a), the localization of electrons between H and S shows the covalent bond between them, while the bond between F and S is mainly ionic in character.

5.4.2. Stability

It is found that Janus single-layer of TaS_2 is dynamically stable. As seen in Fig. 5.4 (b) the phonon band distribution of Janus type single-layer of TaS_2 has 3 acoustics and 12 optical modes. The gap between two different kind modes is 27 cm^{-1}. While out-of-plane modes with frequencies 250 cm^{-1} ($\widetilde{A}_{2u}$), 297 cm^{-1} ($\widetilde{A}_{2u}$), 647 cm^{-1} ($\widetilde{A}_{1g}$), 2160 cm^{-1} ($\widetilde{A}_{1g}$) are non-degenerate, all in-plane characters from optical modes are degenerate with frequencies $\widetilde{E}_g = 74$ cm^{-1}, $\widetilde{E}_g = 236$ cm^{-1}, $\widetilde{E}_u = 317$ cm^{-1}, $\widetilde{E}_g = 503$ cm^{-1}, respectively.

5.4.3. Electronic Structure

Knowledge of the composition of electronic band structure is crucial for understanding electronic and optical procedures in different electronic and optoelectronic devices. As shown in Fig. 5.4 (c), the electronic band diagram of the Janus type of single-layer TaS_2 has a continuous energy distribution at point zero and does not have a gap so it shows metallic character. The graph of PDOS corresponding to the electronic band diagram shows that the greatest contribution in the structure originates from the d orbital of the Ta atoms.

5.5. Mechanical, Piezoelectric, and Thermal Properties

Piezoelectricity is a physical process that occurs in materials owing to the absence of centrosymmetric and generates electric dipole moment when pressure is applied. In materials with mirror asymmetry, the vertical potential gradient is induced and thus shifts

the spin polarization for the opposite momentum plane, resulting in Rashba spin splitting. However, since a piezoelectric material should not be symmetrical, 2D systems that are symmetrical are monitored for piezoelectricity. In order to investigate the effects of piezoelectric, the concepts of linear elastic fracture mechanics are used to examine the effect of electric fields on the fracture behavior of piezoelectric materials. The mathematical explanation of piezoelectricity is to relate stress to the electric field by means of a tensor. Tensor is an algebraic expression when any piezoelectric material is exposed to the electric field or to a mechanical force.

2D materials are elastically characterized by two parameters, in-plane stiffness, C and Poisson ratio, ν. Among 2D ultra-thin materials, graphene has the largest in-plane stiffness (330N/m) due to strong in-plane bonding of C atoms, the in-plane stiffness of TaS_2 (120.5 N/m) is found to be relatively closer to single-layer MoS_2 (122 N/m)(Yagmurcukardes *et al.*, 2016), which is known to be softer than graphene. Hydrogenation and fluorination are found to soften single-layer TaS_2 with C values are 88.0 and 89.7 N/m, respectively. As the Janus type structure is constructed, the in-plane Ta-S bonds weaken and the in-plane stiffness decreases to 65.3 N/m which is almost half of that of bare TaS_2. Poisson ratio, the ratio of transverse strain to axial strain, is calculated using the formula; $\nu = C_{12}/C_{11}$. As listed in Table 5.2, Poisson ratio for TaS_2, $FTaS_2$ and $HTaS_2$ structures are 0.35, 0.21 and 0.23, respectively. In the case of Janus type TaS_2, Poisson ratio is found to be quite large, 0.47, indicating the larger response to the vertically applied load as compared to other TaS_2 structures.

In addition, there are also two piezoelectric coefficients for describing piezoelectricity in two-dimensional materials, which can be defined as the linear piezoelectric coefficients d_{ij} and relaxed-ion piezoelectric tensor e_{ij}, the sum of ionic ions and electronic energy contribution. For group-III chalcogenide monolayers with point group symmetry D_{3h}, e_{11}, d_{11} are in-plane and e_{31}, d_{31} are out-of-plane coefficients that characterize piezoelectricity. Therefore, piezoelectric strain coefficients d_{11} and d_{31} for the 1H-phase structures are defined by the following formula;

$$d_{11} = \left(\frac{e_{11}}{C_{11} - C_{12}} \right),$$
$$d_{31} = \left(\frac{e_{31}}{C_{11} + C_{12}} \right), \tag{5.1}$$

As listed in Table 5.2, e_{11} value for bare TaS_2 is found to be 3.04 $\times 10^{-10}$ C/m which is smaller than the reported value for single-layer MoS_2 (3.88 $\times 10^{-10}$ C/m). The single-layers of $FTaS_2$ and $HTaS_2$ are found to exhibit much lower e_{11} values, 1.24 $\times 10^{-10}$
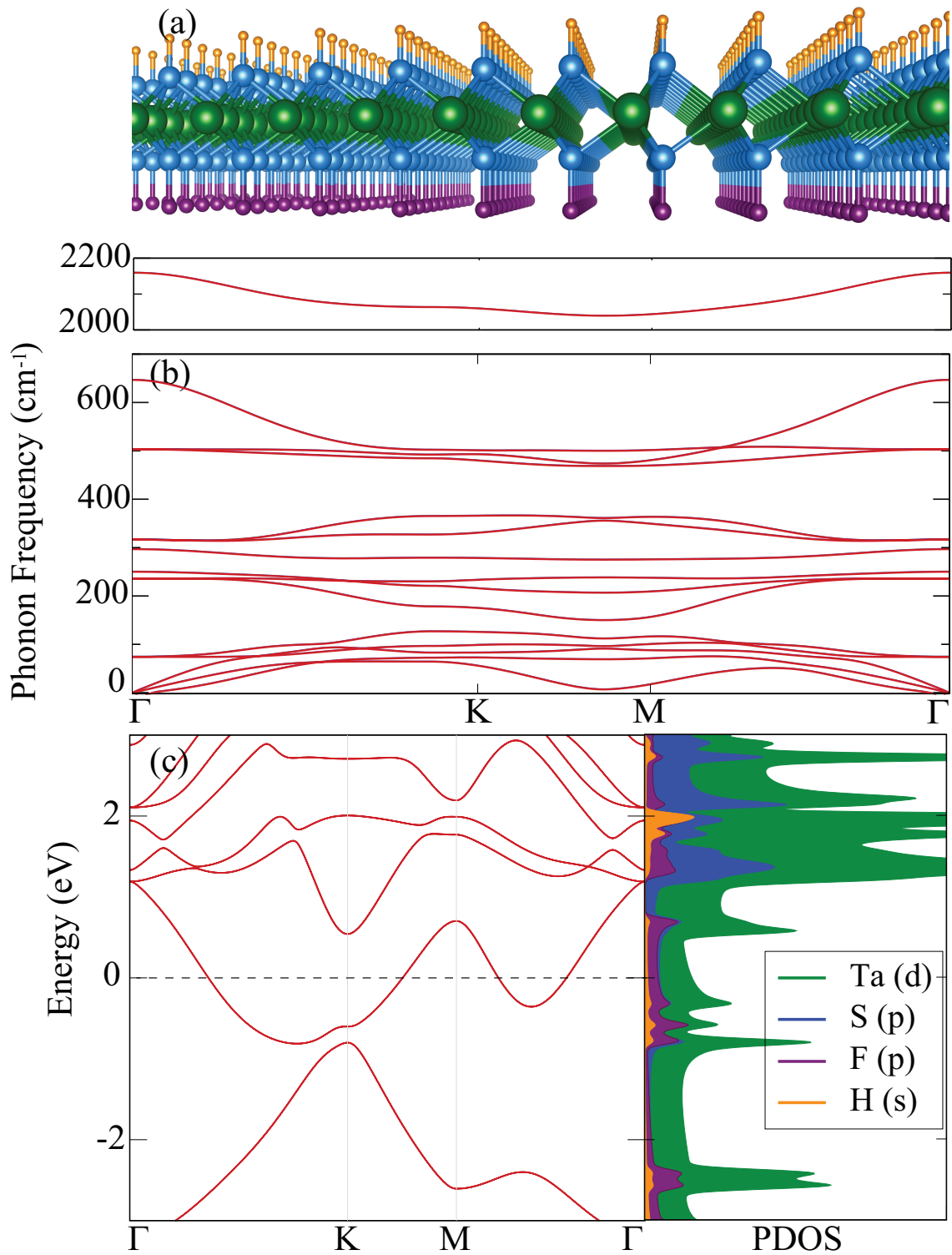
Figure 5.4. Perspective side view of Janus TaS_2. Phonon band diagrams of Janus TaS_2. Electronic band structure and PDOS of Janus TaS_2.

Table 5.2. The calculated parameters for single-layers of TaS_2, $FTaS_2$, $HTaS_2$, and $HTaS_2F$ are: work function, Φ; in-plane stiffness, C; the relaxed-ion piezo-electric stress, e_{ij}; the corresponding piezoelectric strain coefficients, d_{ij}; and Poisson ratio, ν.

	Φ_{Ta-S} (eV)	Φ_{F-S} (eV)	Φ_{H-S} (eV)	C_{11} (Nm^{-1})	C_{12} (Nm^{-1})	C (Nm^{-1})
TaS_2	5.94	-	-	120.5	42.0	104.9
$FTaS_2$	5.39	5.64	-	91.9	19.0	88.0
$HTaS_2$	5.50	-	1.86	94.8	21.9	89.7
$HTaS_2F$	-	9.35	3.40	84.0	39.6	65.3
	e_{11} (Cm$^{-1}\times10^{-10}$)	e_{31} (Cm$^{-1}\times10^{-10}$)	d_{11} (pmV^{-1})	d_{31} (pmV^{-1})	ν $-$	
TaS_2	3.04	0.00	3.87	0.00	0.35	
$FTaS_2$	1.24	0.74	1.70	0.67	0.21	
$HTaS_2$	1.51	0.05	2.07	0.04	0.23	
$HTaS_2F$	1.26	0.76	2.84	0.61	0.47	

and 1.51×10^{-10} C/m, respectively, due to extra charge transfer from Ta atom to adsorbed F or H atoms that weakens the in-plane polarization in the crystal. In addition, e_{11} for the Janus $HTaS_2F$ single-layer (1.26×10^{-10} C/m) is found to be closer to that of $HTaS_2$. The broken out-of-plane symmetry in single-layers of $FTaS_2$, $HTaS_2$, and $HTaS_2F$ creates a net dipole moment along the out-of-plane directions resulting in non-zero e_{31} elements. The calculated values for $FTaS_2$ and $HTaS_2F$ are close to each other (0.74×10^{-10} and 0.76×10^{-10} C/m, respectively) while it is found to be very small for $HTaS_2$, 0.05×10^{-10} C/m. Apparently, the lack of extra charge transfer between H and S atoms does not add any contribution to the out-of-plane polarization. However, strong electronegativity of F atoms result in high charge depletion and considerably large out-of-plane piezoelectricity.

5.6. Thermal Properties

One important property of a material is its thermal behaviors which is important for applications in nanoscale devices at finite temperatures. As shown in Fig.5.6, all four heat capacity curves increase rapidly in the low temperature regime and asymptotically approach the classical limit of $3Nk_B$ where N and k_B denote the number of atoms and the Boltzmann constant, respectively. It is known that the low temperature behavior of the heat capacity of the 2D crystals is determined by the phonon modes. In bare and functionalized TaS_2 structures, the low-temperature thermal excitations take place in acoustic phonon branches and consequently the heat capacity is governed by the acoustic phonons.
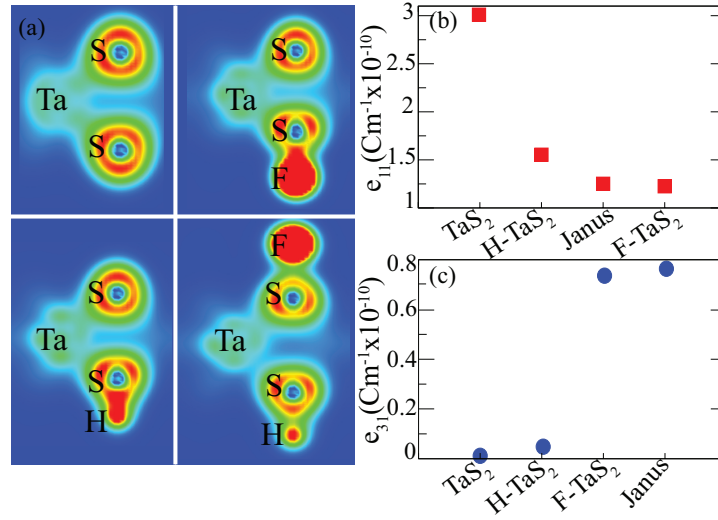
Figure 5.5. Contour plots of the total charge density ρT in the plane passing through S-Ta-S, S-Ta-S-H, S-Ta-S-F, F-S-Ta-S-H atom, respectively.

As the heat capacities of single-layer TaS_2 structures are compared, it is seen that Janus $HTaS_2F$ has the highest heat capacity either at low or high temperatures. While at high temperatures single-layer TaS_2 has the lowest heat capacity, the heat capacity of single-layer $HTaS_2$ is the smallest at low temperatures. In addition, at the low temperature limit, the rise of the heat capacity of single-layer TaS_2 structures is not linear with the temperature instead the relation is more likely quadratic. As the temperature dependence of the specific heat is $T^{2/n}$ at low temperatures in 2D materials, quadratic-like behavior heat capacity of TaS_2 structures reveals the number n to be ≈ 1. Since the frequency of a phonon mode scales with the momentum, q, as $\omega = q^n$, the dispersion of phonon frequency is found to be $\omega = q$ that indicates the contribution of LA and TA acoustical modes to the low-temperature heat capacity of TaS_2 structures.
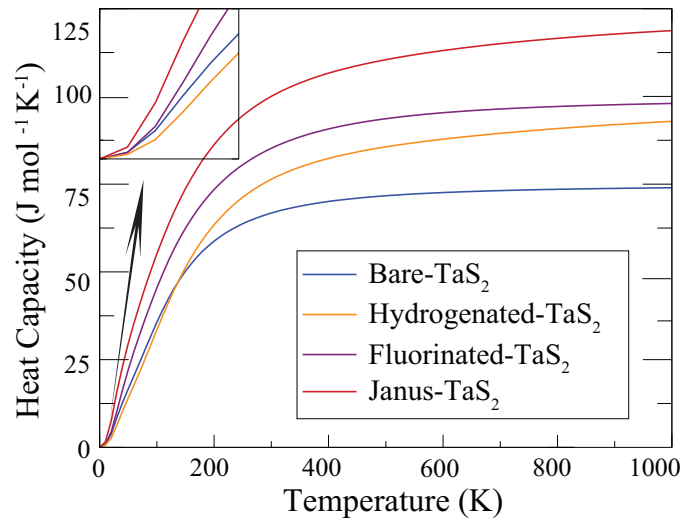
Figure 5.6. Heat capacity of single-layer of bare-TaS$_2$, hydrogenated TaS$_2$, fluorinated TaS$_2$, and Janus TaS$_2$.

CHAPTER 6

CONCLUSIONS

In this study, we investigated thickness dependency of structural, vibrational and electronic properties of the 1T-PtSe$_2$ by performing first-principles calculations. First, it was found that the monolayer of platinum diselenide forms a dynamically stable hexagonal 1T phase, and the monolayer is an indirect band gap semiconductor. The electronic nature of the monolayer structure changes negligibly under biaxial tensile deformation revealing the robust semiconductor character of the material. In addition, electronic dispersion calculations on crystals of various thickness showed that while monolayer and bilayer structures of 1T-PtSe$_2$ are indirect band-gap semiconductors, all thicker structures exhibit metallic character.

The layer-dependent vibrational spectra of the 1T-PtSe$_2$ structures reveal that Raman active shear mode, layer-breathing mode, E$_g$ mode, and A$_{1g}$ mode display significant shifts indicating the increasing layer-layer interaction. Moreover, Raman intensity of the E$_g$ phonon branch is found to be quite sensitive to the material thickness and therefore it can be used for determination of number of layers by Raman spectroscopy.

In the present work, the structural, electronic, and vibrational properties of the single-layers of PtX$_2$ and Janus type XPtY (where X/Y=S, Se, Te) were investigated by performing *ab*-initio calculations. It was shown that single-layer PtX$_2$ structures are dynamically stable structures in 1T phase and display three characteristic Raman active phonon modes at the Γ point that can be observed by Raman measurements. Furthermore, it was found that formation of Janus type platinum dichalcogenide crystals having two different atoms at opposite surfaces is possible via chalcogen exchange and all XPtYs are dynamically stable. In addition, in their Raman spectrum, Janus XPtY structures exhibit additional three Raman-active modes stemming from broken out-of-plane symmetry. Electronically, similar to their binary analogs, all Janus type platinum chalcogenide structures were The vdW heterostructures of were also investigated. It was found that 36 possible vdW heterostructures create ultra-thin heterojunctions of type-I, II, and III. Our study reveal that Janus type platinum dichalcogenide crystals are novel stable materials having wide-range of electronic character.

we investigated the structural, vibrational, electronic, piezoelectric and properties of single-layer bare, fluorinated, hydrogenated, and Janus type TaS$_2$ by performing state-

of-the-art density functional theory calculations. Firstly, it was found that all single-layer TaS_2 crystal structures show hexagonal symmetry with $P\bar{6}m3$ space groups.

Furthermore, we also shown that single-layer of TaS_2 can be chemically functionalized by hydrogenation and fluorination. Fluorination of TaS_2 did not change the structural properties. It was shown that TaS_2 can acquire a teflon-like property and the electronic properties of TaS_2 can be tuned with the effect of fluorination. It was found that fluorinated TaS_2 is a indirect semiconductor with 0.65 eV band gap while bare TaS_2 is a metal.

The structural properties of the hydrogenated TaS_2 were found to be the same as the structural properties of the TaS_2. However, the electronic properties of TaS_2 were found to differ. We shown that the electronic band gap of TaS_2 was opened by the effect of hydrogenation and the hydrogenated TaS_2 also is an indirect band gap semiconductor like fluorinated TaS_2.

Janus material was formed by fluorinating one side of TaS_2 and hydrogenating the other side. Janus TaS_2 was found to have the same characteristics as the bare TaS_2 in terms of structural properties. Janus TaS_2 has been found to be dynamically stable. According to the electronic band diagram, Janus was shown to be metal. In the PDOS graph corresponding to the electronic band diagram emphasized that the most contribution came from the d orbitals of the Ta atom.

Finally, single-layer TaS_2 and derivatives were examined in terms of thermal properties. In addition, the elastic and piezoelectric properties of TaS_2 and its derivatives were investigated. It was revealed that the in-plane piezoelectricity of TaS_2 can be increased by the fluorination effect while an additional degree of freedom can be added for piezoelectricity of Janus structures with broken out-of-plane symmetry.

REFERENCES

Akbali, B., A. Yanilmaz, A. Tomak, S. Tongay, C. Çelebi, and H. Sahin (2017). Few-layer mos2 as nitrogen protective barrier. *Nanotechnology 28*(41), 415706.

Ataca, C., H. Sahin, E. Akturk, and S. Ciraci (2011). Mechanical and electronic properties of mos2 nanoribbons and their defects. *The Journal of Physical Chemistry C 115*(10), 3934–3941.

Ataca, C., H. Sahin, and S. Ciraci (2012). Stable, single-layer mx2 transition-metal oxides and dichalcogenides in a honeycomb-like structure. *The Journal of Physical Chemistry C 116*(16), 8983–8999.

Ben-Melech Stan, G. and M. Caspary Toroker (2018). Lateral chemical bonding in two-dimensional transition-metal dichalcogenide metal/semiconductor heterostructures. *The Journal of Physical Chemistry C 122*(10), 5401–5410.

Brodie, B. C. (1859). Xiii. on the atomic weight of graphite. *Philosophical Transactions of the Royal Society of London* (149), 249–259.

Cahangirov, S., M. Topsakal, E. Aktürk, H. Şahin, and S. Ciraci (2009). Two-and one-dimensional honeycomb structures of silicon and germanium. *Physical review letters 102*(23), 236804.

Castellanos-Gomez, A., M. Poot, G. A. Steele, H. S. van der Zant, N. Agraït, and G. Rubio-Bollinger (2012). Elastic properties of freely suspended mos2 nanosheets. *Advanced Materials 24*(6), 772–775.

Cheng, Y., Z. Zhu, M. Tahir, and U. Schwingenschlögl (2013). Spin-orbit–induced spin splittings in polar transition metal dichalcogenide monolayers. *EPL (Europhysics Letters) 102*(5), 57001.

Chernikov, A., A. M. van der Zande, H. M. Hill, A. F. Rigosi, A. Velauthapillai, J. Hone, and T. F. Heinz (2015). Electrical tuning of exciton binding energies in monolayer ws 2. *Physical review letters 115*(12), 126802.

Chhowalla, M., H. S. Shin, G. Eda, L.-J. Li, K. P. Loh, and H. Zhang (2013). The chemistry of two-dimensional layered transition metal dichalcogenide nanosheets. *Nature chemistry 5*(4), 263.

Chia, X., A. Adriano, P. Lazar, Z. Sofer, J. Luxa, and M. Pumera (2016). Layered platinum dichalcogenides (pts2, ptse2, and ptte2) electrocatalysis: monotonic dependence on the chalcogen size. *Advanced Functional Materials 26*(24), 4306–4318.

Chuang, H.-J., B. Chamlagain, M. Koehler, M. M. Perera, J. Yan, D. Mandrus, D. Tománek, and Z. Zhou (2016). Low-resistance 2d/2d ohmic contacts: A universal approach to high-performance wse2, mos2, and mose2 transistors. *Nano letters 16*(3), 1896–1902.

Ciarrocchi, A., A. Avsar, D. Ovchinnikov, and A. Kis (2018). Thickness-modulated metal-to-semiconductor transformation in a transition metal dichalcogenide. *Nature communications 9*(1), 919.

Coleman, J. N., M. Lotya, A. OâNeill, S. D. Bergin, P. J. King, U. Khan, K. Young, A. Gaucher, S. De, R. J. Smith, *et al.* (2011). Two-dimensional nanosheets produced by liquid exfoliation of layered materials. *Science 331*(6017), 568–571.

Dong, L., J. Lou, and V. B. Shenoy (2017). Large in-plane and vertical piezoelectricity in janus transition metal dichalchogenides. *ACS nano 11*(8), 8242–8248.

Du, J., P. Song, L. Fang, T. Wang, Z. Wei, J. Li, and C. Xia (2018). Elastic, electronic and optical properties of the two-dimensional ptx2 (x= s, se, and te) monolayer. *Applied Surface Science 435*, 476–482.

Elias, D. C., R. R. Nair, T. Mohiuddin, S. Morozov, P. Blake, M. Halsall, A. C. Ferrari, D. Boukhvalov, M. Katsnelson, A. Geim, *et al.* (2009). Control of graphene's properties by reversible hydrogenation: evidence for graphane. *Science 323*(5914), 610–613.

Fuhrer, M. S., C. N. Lau, and A. H. MacDonald (2010). Graphene: materially better carbon. *MRS bulletin 35*(4), 289–295.

Geim, A. K. and I. V. Grigorieva (2013). Van der waals heterostructures. *Na-*

ture 499(7459), 419.

Geremew, A. K., S. Rumyantsev, F. Kargar, B. Debnath, A. Nosek, M. A. Bloodgood, M. Bockrath, T. T. Salguero, R. K. Lake, and A. A. Balandin (2019). Bias-voltage driven switching of the charge-density-wave and normal metallic phases in 1t-tas2 thin-film devices. *ACS nano 13*(6), 7231–7240.

Gong, C., H. Zhang, W. Wang, L. Colombo, R. M. Wallace, and K. Cho (2013). Band alignment of two-dimensional transition metal dichalcogenides: Application in tunnel field effect transistors. *Applied Physics Letters 103*(5), 053513.

Grimme, S. (2006). Semiempirical gga-type density functional constructed with a long-range dispersion correction. *Journal of computational chemistry 27*(15), 1787–1799.

Guo, G. and W. Liang (1986). The electronic structures of platinum dichalcogenides: Pts2, ptse2 and ptte2. *Journal of Physics C: Solid State Physics 19*(7), 995.

Guzman, D. M. and A. Strachan (2014). Role of strain on electronic and mechanical response of semiconducting transition-metal dichalcogenide monolayers: An ab-initio study. *Journal of Applied Physics 115*(24), 243701.

Haastrup, S., M. Strange, M. Pandey, T. Deilmann, P. S. Schmidt, N. F. Hinsche, M. N. Gjerding, D. Torelli, P. M. Larsen, A. C. Riis-Jensen, *et al.* (2018). The computational 2d materials database: high-throughput modeling and discovery of atomically thin crystals. *2D Materials 5*(4), 042002.

Henkelman, G., A. Arnaldsson, and H. Jónsson (2006). A fast and robust algorithm for bader decomposition of charge density. *Computational Materials Science 36*(3), 354–360.

Hinsche, N. F. and K. S. Thygesen (2017). Electron–phonon interaction and transport properties of metallic bulk and monolayer transition metal dichalcogenide tas2. *2D Materials 5*(1), 015009.

Huo, N., J. Kang, Z. Wei, S.-S. Li, J. Li, and S.-H. Wei (2014). Novel and enhanced optoelectronic performances of multilayer mos2–ws2 heterostructure transistors. *Advanced Functional Materials 24*(44), 7025–7031.

Island, J. O., A. Kuc, E. H. Diependaal, R. Bratschitsch, H. S. van der Zant, T. Heine, and A. Castellanos-Gomez (2016). Precise and reversible band gap tuning in single-layer mose 2 by uniaxial strain. *Nanoscale 8*(5), 2589–2593.

İyikanat, F., A. Kandemir, H. Ozaydin, R. T. Senger, and H. Sahin (2017). Hydrogenation-driven phase transition in single-layer tise2. *Nanotechnology 28*(49), 495709.

Jariwala, D., V. K. Sangwan, L. J. Lauhon, T. J. Marks, and M. C. Hersam (2014). Emerging device applications for semiconducting two-dimensional transition metal dichalcogenides. *ACS nano 8*(2), 1102–1120.

Joshi, S., F. Bischoff, R. Koitz, D. Ecija, K. Seufert, A. P. Seitsonen, J. Hutter, K. Diller, J. I. Urgel, H. Sachdev, *et al.* (2013). Control of molecular organization and energy level alignment by an electronically nanopatterned boron nitride template. *ACS nano 8*(1), 430–442.

Kahraman, Z., A. Kandemir, M. Yagmurcukardes, and H. Sahin (2019). Single-layer janus-type platinum dichalcogenides and their heterostructures. *The Journal of Physical Chemistry C 123*(7), 4549–4557.

Kandemir, A. and H. Sahin (2018). Janus single layers of in 2 sse: A first-principles study. *Physical Review B 97*(15), 155410.

Kang, J., H. Sahin, and F. M. Peeters (2015). Mechanical properties of monolayer sulphides: a comparative study between mos 2, hfs 2 and tis 3. *Physical Chemistry Chemical Physics 17*(41), 27742–27749.

Kim, K. K., A. Hsu, X. Jia, S. M. Kim, Y. Shi, M. Hofmann, D. Nezich, J. F. Rodriguez-Nieva, M. Dresselhaus, T. Palacios, *et al.* (2011). Synthesis of monolayer hexagonal boron nitride on cu foil using chemical vapor deposition. *Nano letters 12*(1), 161–166.

Kliche, G. (1985). Far-infrared and x-ray investigations of the mixed platinum dichalcogenides pts2- xsex, ptse2- xtex, and pts2- xtex. *Journal of Solid State Chemistry 56*(1), 26–31.

Koperski, M., K. Nogajewski, A. Arora, V. Cherkez, P. Mallet, J.-Y. Veuillen, J. Marcus,

P. Kossacki, and M. Potemski (2015). Single photon emitters in exfoliated wse 2 structures. *Nature nanotechnology 10*(6), 503.

Kresse, G. and J. Furthmuller (1996). Efficient iterative schemes for ab initio total-energy calculations using a plane-wave basis set. *Physical review B 54*(16), 11169.

Kresse, G. and J. Hafner (1993). Ab initio molecular dynamics for liquid metals. *Physical Review B 47*(1), 558.

Late, D. J., B. Liu, J. Luo, A. Yan, H. R. Matte, M. Grayson, C. Rao, and V. P. Dravid (2012). Gas and gase ultrathin layer transistors. *Advanced Materials 24*(26), 3549–3554.

Lee, C., H. Yan, L. E. Brus, T. F. Heinz, J. Hone, and S. Ryu (2010). Anomalous lattice vibrations of single-and few-layer mos2. *ACS nano 4*(5), 2695–2700.

Lee, J., J. Huang, B. G. Sumpter, and M. Yoon (2017). Strain-engineered optoelectronic properties of 2d transition metal dichalcogenide lateral heterostructures. *2D Materials 4*(2), 021016.

Li, L., W. Wang, Y. Chai, H. Li, M. Tian, and T. Zhai (2017). Few-layered pts2 phototransistor on h-bn with high gain. *Advanced Functional Materials 27*(27), 1701011.

Li, Y., Z. Zhu, J. Yu, and B. Ding (2015). Carbon nanotubes enhanced fluorinated polyurethane macroporous membranes for waterproof and breathable application. *ACS applied materials & interfaces 7*(24), 13538–13546.

Lu, A.-Y., H. Zhu, J. Xiao, C.-P. Chuu, Y. Han, M.-H. Chiu, C.-C. Cheng, C.-W. Yang, K.-H. Wei, Y. Yang, *et al.* (2017). Janus monolayers of transition metal dichalcogenides. *Nature nanotechnology 12*(8), 744.

Lu, Q., Y. Yu, Q. Ma, B. Chen, and H. Zhang (2016). 2d transition-metal-dichalcogenide-nanosheet-based composites for photocatalytic and electrocatalytic hydrogen evolution reactions. *Advanced Materials 28*(10), 1917–1933.

Lu, X., M. I. B. Utama, J. Lin, X. Gong, J. Zhang, Y. Zhao, S. T. Pantelides, J. Wang, Z. Dong, Z. Liu, *et al.* (2014). Large-area synthesis of monolayer and few-layer mose2

films on sio2 substrates. *Nano letters 14*(5), 2419–2425.

Ma, Q., W. Yu, X. Dong, J. Wang, and G. Liu (2014). Janus nanobelts: fabrication, structure and enhanced magnetic–fluorescent bifunctional performance. *Nanoscale 6*(5), 2945–2952.

Mak, K. F., C. Lee, J. Hone, J. Shan, and T. F. Heinz (2010). Atomically thin mos 2: a new direct-gap semiconductor. *Physical review letters 105*(13), 136805.

Mas-Balleste, R., C. Gomez-Navarro, J. Gomez-Herrero, and F. Zamora (2011). 2d materials: to graphene and beyond. *Nanoscale 3*(1), 20–30.

Molina-Sanchez, A. and L. Wirtz (2011). Phonons in single-layer and few-layer mos 2 and ws 2. *Physical Review B 84*(15), 155413.

Nair, R. R., W. Ren, R. Jalil, I. Riaz, V. G. Kravets, L. Britnell, P. Blake, F. Schedin, A. S. Mayorov, S. Yuan, *et al.* (2010). Fluorographene: a two-dimensional counterpart of teflon. *small 6*(24), 2877–2884.

Nasr Esfahani, D., O. Leenaerts, H. Sahin, B. Partoens, and F. Peeters (2015). Structural transitions in monolayer mos2 by lithium adsorption. *The Journal of Physical Chemistry C 119*(19), 10602–10609.

Novoselov, K., A. Mishchenko, A. Carvalho, and A. C. Neto (2016). 2d materials and van der waals heterostructures. *Science 353*(6298), aac9439.

Novoselov, K. S., A. K. Geim, S. V. Morozov, D. Jiang, Y. Zhang, S. V. Dubonos, I. V. Grigorieva, and A. A. Firsov (2004). Electric field effect in atomically thin carbon films. *science 306*(5696), 666–669.

Nye, J. F. *et al.* (1985). *Physical properties of crystals: their representation by tensors and matrices*. Oxford university press.

Perdew, J. P., K. Burke, and M. Ernzerhof (1996). Generalized gradient approximation made simple. *Physical review letters 77*(18), 3865.

Perdew, J. P. and A. Zunger (1981). Self-interaction correction to density-functional ap-

proximations for many-electron systems. *Physical Review B 23*(10), 5048.

Qian, X., J. Liu, L. Fu, and J. Li (2014). Quantum spin hall effect in two-dimensional transition metal dichalcogenides. *Science 346*(6215), 1344–1347.

Ramakrishna Matte, H., A. Gomathi, A. K. Manna, D. J. Late, R. Datta, S. K. Pati, and C. Rao (2010). Mos2 and ws2 analogues of graphene. *Angewandte Chemie International Edition 49*(24), 4059–4062.

Robinson, J. T., J. S. Burgess, C. E. Junkermeier, S. C. Badescu, T. L. Reinecke, F. K. Perkins, M. K. Zalalutdniov, J. W. Baldwin, J. C. Culbertson, P. E. Sheehan, *et al.* (2010). Properties of fluorinated graphene films. *Nano letters 10*(8), 3001–3005.

Şahin, H., M. Topsakal, and S. Ciraci (2011). Structures of fluorinated graphene and their signatures. *Physical Review B 83*(11), 115432.

Sajjad, M., E. Montes, N. Singh, and U. Schwingenschlögl (2017). Superior gas sensing properties of monolayer ptse2. *Advanced Materials Interfaces 4*(5), 1600911.

Sajjad, M., N. Singh, and U. Schwingenschlögl (2018). Strongly bound excitons in monolayer pts2 and ptse2. *Applied Physics Letters 112*(4), 043101.

Schuller, I. K. (1980). New class of layered materials. *Physical review letters 44*(24), 1597.

Shi, J., X. Wang, S. Zhang, L. Xiao, Y. Huan, Y. Gong, Z. Zhang, Y. Li, X. Zhou, M. Hong, *et al.* (2017). Two-dimensional metallic tantalum disulfide as a hydrogen evolution catalyst. *Nature communications 8*(1), 958.

Sofo, J. O., A. S. Chaudhari, and G. D. Barber (2007). Graphane: A two-dimensional hydrocarbon. *Physical Review B 75*(15), 153401.

Soled, S., A. Wold, and O. Gorochov (1976). Crystal growth and characterization of several platinum sulfoselenides. *Materials Research Bulletin 11*(8), 927–932.

Splendiani, A., L. Sun, Y. Zhang, T. Li, J. Kim, C.-Y. Chim, G. Galli, and F. Wang (2010). Emerging photoluminescence in monolayer mos2. *Nano letters 10*(4), 1271–1275.

Sreepal, V., M. Yagmurcukardes, K. S. Vasu, D. J. Kelly, S. F. Taylor, V. G. Kravets, Z. Kudrynskyi, Z. D. Kovalyuk, A. Patanè, A. N. Grigorenko, *et al.* (2019). Two-dimensional covalent crystals by chemical conversion of thin van der waals materials. *Nano letters 19*(9), 6475–6481.

Tan, C. and H. Zhang (2015). Two-dimensional transition metal dichalcogenide nanosheet-based composites. *Chemical Society Reviews 44*(9), 2713–2731.

Thompson, A., F. Gamble, and R. Koehler Jr (1972). Effects of intercalation on electron transport in tantalum disulfide. *Physical Review B 5*(8), 2811.

Togo, A., F. Oba, and I. Tanaka (2008). First-principles calculations of the ferroelastic transition between rutile-type and cacl 2-type sio 2 at high pressures. *Physical Review B 78*(13), 134106.

Ullah, K., S. Ye, S.-B. Jo, L. Zhu, K.-Y. Cho, and W.-C. Oh (2014). Optical and photocatalytic properties of novel heterogeneous ptse2–graphene/tio2 nanocomposites synthesized via ultrasonic assisted techniques. *Ultrasonics sonochemistry 21*(5), 1849–1857.

Vogt, P., P. De Padova, C. Quaresima, J. Avila, E. Frantzeskakis, M. C. Asensio, A. Resta, B. Ealet, and G. Le Lay (2012). Silicene: compelling experimental evidence for graphenelike two-dimensional silicon. *Physical review letters 108*(15), 155501.

Wang, J., S. Chen, X. Quan, and H. Yu (2018). Fluorine-doped carbon nanotubes as an efficient metal-free catalyst for destruction of organic pollutants in catalytic ozonation. *Chemosphere 190*, 135–143.

Wang, Q. H., K. Kalantar-Zadeh, A. Kis, J. N. Coleman, and M. S. Strano (2012). Electronics and optoelectronics of two-dimensional transition metal dichalcogenides. *Nature nanotechnology 7*(11), 699.

Wang, Y., L. Li, W. Yao, S. Song, J. Sun, J. Pan, X. Ren, C. Li, E. Okunishi, Y.-Q. Wang, *et al.* (2015). Monolayer ptse2, a new semiconducting transition-metal-dichalcogenide, epitaxially grown by direct selenization of pt. *Nano letters 15*(6), 4013–4018.

Wehling, T., K. Novoselov, S. Morozov, E. Vdovin, M. Katsnelson, A. Geim, and A. Lichtenstein (2008). Molecular doping of graphene. *Nano letters 8*(1), 173–177.

Woods, J. M., Y. Jung, Y. Xie, W. Liu, Y. Liu, H. Wang, and J. J. Cha (2016). One-step synthesis of mos2/ws2 layered heterostructures and catalytic activity of defective transition metal dichalcogenide films. *ACS nano 10*(2), 2004–2009.

Wu, Y., X. Lin, Z. Wu, H. Moìhwald, and Q. He (2014). Self-propelled polymer multi-layer janus capsules for effective drug delivery and light-triggered release. *ACS applied materials & interfaces 6*(13), 10476–10481.

Yagmurcukardes, M., C. Bacaksiz, R. Senger, and H. Sahin (2017). Hydrogen-induced structural transition in single layer res2. *2D Materials 4*(3), 035013.

Yagmurcukardes, M., C. Bacaksiz, E. Unsal, B. Akbali, R. Senger, and H. Sahin (2018). Strain mapping in single-layer two-dimensional crystals via raman activity. *Physical Review B 97*(11), 115427.

Yagmurcukardes, M., R. Senger, F. Peeters, and H. Sahin (2016). Mechanical properties of monolayer gas and gase crystals. *Physical Review B 94*(24), 245407.

Yao, W., E. Wang, H. Huang, K. Deng, M. Yan, K. Zhang, K. Miyamoto, T. Okuda, L. Li, Y. Wang, *et al.* (2017). Direct observation of spin-layer locking by local rashba effect in monolayer semiconducting ptse 2 film. *Nature communications 8*, 14216.

Ye, S. and W.-C. Oh (2016). Demonstration of enhanced the photocatalytic effect with ptse2 and tio2 treated large area graphene obtained by cvd method. *Materials Science in Semiconductor Processing 48*, 106–114.

Yeo, J. S., J. J. Vittal, W. Henderson, and T. A. Hor (2002). Exploring the lewis basicity of the metalloligand [pt 2 (μ-se) 2 (pph 3) 4] on metal substrates by electrospray mass spectrometry. synthesis, characterization and structural studies of new platinum selenido phosphine complexes containing the {Pt 2 Se 2} core. *Journal of the Chemical Society, Dalton Transactions* (3), 328–336.

Yim, C., K. Lee, N. McEvoy, M. OâBrien, S. Riazimehr, N. C. Berner, C. P. Cullen, J. Kotakoski, J. C. Meyer, M. C. Lemme, *et al.* (2016). High-performance hybrid electronic

devices from layered ptse2 films grown at low temperature. *ACS nano 10*(10), 9550–9558.

Yin, Z., H. Li, H. Li, L. Jiang, Y. Shi, Y. Sun, G. Lu, Q. Zhang, X. Chen, and H. Zhang (2011). Single-layer mos2 phototransistors. *ACS nano 6*(1), 74–80.

Yu, Y., F. Yang, X. F. Lu, Y. J. Yan, Y.-H. Cho, L. Ma, X. Niu, S. Kim, Y.-W. Son, D. Feng, *et al.* (2015). Gate-tunable phase transitions in thin flakes of 1t-tas 2. *Nature nanotechnology 10*(3), 270.

Zeng, L.-H., S.-H. Lin, Z.-J. Li, Z.-X. Zhang, T.-F. Zhang, C. Xie, C.-H. Mak, Y. Chai, S. P. Lau, L.-B. Luo, *et al.* (2018). Fast, self-driven, air-stable, and broadband photodetector based on vertically aligned ptse2/gaas heterojunction. *Advanced Functional Materials 28*(16), 1705970.

Zhang, J., S. Jia, I. Kholmanov, L. Dong, D. Er, W. Chen, H. Guo, Z. Jin, V. B. Shenoy, L. Shi, *et al.* (2017). Janus monolayer transition-metal dichalcogenides. *ACS nano 11*(8), 8192–8198.

Zhang, X., W. Han, J. Wu, S. Milana, Y. Lu, Q. Li, A. C. Ferrari, and P. Tan (2013). Raman spectroscopy of shear and layer breathing modes in multilayer mos 2. *Physical Review B 87*(11), 115413.

Zhang, Y., T.-R. Chang, B. Zhou, Y.-T. Cui, H. Yan, Z. Liu, F. Schmitt, J. Lee, R. Moore, Y. Chen, *et al.* (2014). Direct observation of the transition from indirect to direct bandgap in atomically thin epitaxial mose 2. *Nature nanotechnology 9*(2), 111.

Zhang, Z.-X., L.-H. Zeng, X.-W. Tong, Y. Gao, C. Xie, Y. H. Tsang, L.-B. Luo, and Y.-C. Wu (2018). Ultrafast, self-driven, and air-stable photodetectors based on multilayer ptse2/perovskite heterojunctions. *The journal of physical chemistry letters 9*(6), 1185–1194.

Zhao, G. and M. Pumera (2014). Geometric asymmetry driven janus micromotors. *Nanoscale 6*(19), 11177–11180.

Zhao, J., C. R. Cabrera, Z. Xia, and Z. Chen (2016). Single- sided fluorine–functionalized graphene: A metal–free electrocatalyst with high efficiency for oxygen reduction re-

action. *Carbon 104*, 56–63.

Zhao, Y., J. Qiao, P. Yu, Z. Hu, Z. Lin, S. P. Lau, Z. Liu, W. Ji, and Y. Chai (2016). Extraordinarily strong interlayer interaction in 2d layered pts2. *Advanced Materials 28*(12), 2399–2407.

Zhao, Y., J. Qiao, Z. Yu, P. Yu, K. Xu, S. P. Lau, W. Zhou, Z. Liu, X. Wang, W. Ji, *et al.* (2017). High-electron-mobility and air-stable 2d layered ptse2 fets. *Advanced Materials 29*(5), 1604230.

Zhuang, H. L. and R. G. Hennig (2012). Electronic structures of single-layer boron pnictides. *Applied Physics Letters 101*(15), 153109.